Fakultät für Physik und Astronomie
Ruprecht-Karls-Universität Heidelberg

Bachelor thesis in physics submitted by

Jakob Krummeich

and written at the

Max Planck Institute for Nuclear Physics

Heidelberg

12.09.2019

Development of a cooling system for mirrors in an UHV chamber

Adviser and first examiner:	Priv.-Doz. Dr. José Ramón Crespo López-Urrutia
Second examiner:	Prof. Dr. Thomas Pfeifer

Abstract

A cooling system for mirrors of an enhancement cavity is developed. The cavity is used to transfer an infrared frequency comb into the XUV regime using high-harmonic generation. Complementarily, a temperature measurement setup is assembled. An experiment is carried out to determine heating rates of the mirrors and test the temperature measurement.

Contents

1 Introduction

The importance of the interaction of electromagnetic radiation with atomic systems can hardly be overstated. For example, the investigation of hydrogen's spectral lines contributed significantly to the development of quantum mechanics. Today, research in the field of atomic physics is still ongoing and arguably more relevant than ever. Atomic systems are examined very precisely to find hints for 'new physics', for example with atomic clocks [1]. For instance, these experiments can test the variation of fundamental constants.
In recent years, highly charged ions (HCI) have come into focus. They offer reduced sensitivity to external perturbations [2] and are particularly important since most of the baryonic matter in the universe is highly ionized [3]. For astrophysical observations it is therefore crucial to have accurate spectroscopic comparison data of highly charged ions. Since many of the transitions of HCI are located in the extreme ultraviolet (XUV) regime, it is necessary to have access to a precise light source in this energy range. A frequency comb in the ultraviolet regime can serve as such a source.
A frequency comb consists of a mode-locked laser which emits a train of ultrashort light pulses [4]. In the frequency domain this corresponds to discrete and evenly spaced frequencies [5] which enables high precision spectroscopy. Typically, the spectrum of these combs does not reach into the XUV-region. However, this can be accomplished by high-harmonic generation (HHG) [6] of the fundamental near infrared frequency comb laser [7]. Hereby, odd number multiples of the fundamental frequencies reach into the XUV spectral region. The uniform spacing of frequencies can be preserved, so that high precision measurements in the XUV region of transitions in HCI will be possible for the first time.

High-harmonic generation requires very high laser intensities. To facilitate this prerequisite at high repetition rates, it is necessary to make use of an enhancement cavity. The laser light to generate high-harmonics in such a cavity is send on a round trip of exactly the right length so that consecutive pulses interfere constructively, thereby increasing the peak and average light intensities. Due to the constructive interference, the power in the cavity can build up to several kW. Even cavity mirrors with very low absorptance therefore can possibly heat up when the cavity is operational for a long period of time.

In this work we develop a cooling system for the mirrors of a laser cavity which

is intended to realize a frequency comb in the extreme ultraviolet regime by high harmonic generation. The frequency comb is aimed at performing high precision spectroscopy of HCI. Additionally and complementarily, a temperature measurement is designed and heating of the cavity mirrors investigated.

2 Basics and theory of heat transfer

2.1 Thermal radiation

All bodies with a temperature above absolute zero emit electromagnetic radiation called thermal radiation. In the ideal case of the black-body in thermal equilibrium with the electromagnetic radiation field the spectral distribution of emitted energy only depends on the temperature and is given by the famous Planck-spectrum [9, 8]. Moreover, the emitted radiation of an ideal black-body is diffuse, so that it does not depend on the angle between emitting surface and direction of radiation and an ideal black body shows no reflection of incident radiation [10, 11]. The model of the black-body constitutes an upper bound for the total radiated thermal energy of a body given by the Stefan-Boltzmann law

$$\dot{q}_{\text{radiation}} = \sigma T^4, \tag{2.1}$$

where $\dot{q}_{\text{radiation}}$ is the radiated heat flux per unit surface of the black body, $\sigma = 5.67 \times 10^{-8}\,\mathrm{W/(m^2K^4)}$ is the Stefan-Boltzmann constant and T is the absolute temperature in Kelvin [12].
However, many materials exhibit deviations from the ideal black body behavior, for example by reflection of incident radiation. To rigorously describe thermal radiation of real materials (as opposed to the idealized black-body case) the direction-dependence as well as the wavelength dependence of the emitted radiation has to be taken into account [10]. To accomplish this, one introduces emissivity coefficients, which are dimensionless ratios in relation to the maximum emission given by the black body radiator. The directed spectral emissivity is given by

$$\varepsilon'_\lambda(\lambda, \beta, \phi, T) = \frac{L_\lambda(\lambda, \beta, \phi, T)}{L_{\lambda,\text{black}}(\lambda, T)}, \tag{2.2}$$

where λ is the wavelength of the radiation, β is the polar angle and ϕ is the azimuthal angle. L_λ is the directed spectral radiance of the body in question and $L_{\lambda,\text{black}}$ is the directed spectral radiance of the black body which does not depend on the angles β and ϕ since the black body is a diffuse radiator [10]. The directed spectral emissivity is a distribution over the hemisphere and the wavelengths. After Kirchhoff's laws of thermal radiation, the directed spectral absorptance is equal to the directed spectral emissivity for a non-transparent body [10]:

$$a'_\lambda(\lambda, \beta, \phi, T) = \varepsilon'_\lambda(\lambda, \beta, \phi, T). \tag{2.3}$$

The directed spectral absorptance is a dimensionless quantity which relates the absorption of a body to the maximum absorption given by the black body. Thus, for a black body it is $a'_\lambda(\lambda, \beta, \phi, T) = \varepsilon'_\lambda(\lambda, \beta, \phi, T) = 1$ [10]. ε'_λ and a'_λ are material constants which are difficult to measure exactly due to the dependence on temperature, wavelength and angles. Additionally, slight alteration of the surface, such as oxidation or surface roughness, can lead to very different values.

Often the point of interest are not the directed spectral quantities but the total energy emission over all λ and the total hemisphere. This is obtained by integrating the directed spectral emissivity over the hemisphere and all λ. It is called total hemispheric emissivity or simply emissivity $\varepsilon(T)$ and describes the ratio of the total emitted energy of a body to the maximally possible radiated energy given by the black body at the temperature T where $\varepsilon \leq 1$. Thus it is

$$P_{\text{em. rad.}} = \sigma A \varepsilon(T) T^4, \tag{2.4}$$

where $P_{\text{em. rad.}}$ is the total emitted energy flow at temperature T from a surface A of a body with the emissivity $\varepsilon(T)$. The values of ε vary greatly for different materials and different temperatures. Typical values are $\varepsilon = 0.024$ for tungsten at 25 °C and $\varepsilon = 0.15$ at 1000 °C. For oak wood it is $\varepsilon = 0.9$ at 20 °C [11].

2.1.1 Heat transfer by radiation

An exact description of thermal radiation processes - especially heat transfer by radiation - requires to know the spectral and direction-dependent characteristics of the radiating surfaces. As mentioned above, these are difficult to measure. Additionally, the incoming radiation and the reflection properties need to be known and the specific geometry needs to be taken into consideration. Thus, a thorough calculation of heat transfer is rather difficult. Instead of a rigorous treatment, often a simplified model is used in which $a = \varepsilon$ is assumed [10]. Here, a is the hemispheric total absorptance and describes the ratio of total absorbed energy to total incident radiation. Since it depends on the incoming radiation a is in general not a material constant [10]. However, by assuming $a = \varepsilon$ the absorptance is treated to be independent of the incoming radiation. This simplified model is called gray body [11].
We now consider the case, where a gray body with absolute temperature T, emissivity ε and surface area A exchanges heat by radiation with a black environment of temperature T_e. The gray body emits heat with a rate given by Eq. 2.4 and absorbs heat with a rate of [10]

$$P_{\text{absorbed heat}} = \sigma a A T_{\text{e}}^4 = \sigma \varepsilon A T_{\text{e}}^4. \tag{2.5}$$

Therefore, the net heat flow that is transported via radiation is given by

$$P_{\text{net}} = \sigma \varepsilon A | \left(T^4 - T_{\text{e}}^4 \right) |, \tag{2.6}$$

where the heat flows from the hotter to the colder body. In the idealized case where the gray body is a black radiator $\varepsilon = 1$, this reduces to

$$P_{\text{net, 2 bl. bodies}} = \sigma A | \left(T^4 - T_{\text{e}}^4 \right) | \tag{2.7}$$

Thus we see that the net heat transfer is non-linear in the temperature and proportional to the surface of the body in question.

2.2 Heat conduction and Fourier's law

Heat conduction in a solid body is well described by Fourier's law, which states that the heat flux density $\vec{j_q}$ is proportional to the temperature gradient ∇T. In general, the factor of proportionality depends on the state of the body (for example temperature and chemical composition) as well as the direction of the heat flow. However, for isotropic solids the factor of proportionality is independent of the direction. In this case, Fourier's law is given by

$$\vec{j_q} = -\lambda \cdot \nabla T, \tag{2.8}$$

with $\lambda \in \mathbb{R}, \lambda > 0$ and $\lambda = \lambda(T)$ [10, 12]. In the following, the discussion is limited to this isotropic case. According to Eq. 2.8 heat flows from regions with high temperature to regions with lower temperature and the heat flow is pointed in the direction of the largest gradient. The proportionality factor λ is called thermal or heat conductivity and measures the capability for heat conduction in a material. It varies significantly for different solids, for example at 20 °C copper's heat conductivity is 399 W/(Km) and the thermal conductivity of granite is only 2.9 W/(Km) [10].

2.3 The Heat Equation

Using Fourier's law and the law of energy conservation, a second order partial differential equation which governs heat conduction at room temperature and is

known as Heat Equation can be derived. The law of energy conservation can be stated as a continuity equation

$$\left(\frac{\partial \rho_E}{\partial t}\right) + \nabla \cdot \vec{j_E} = 0, \tag{2.9}$$

where ρ_E is the energy density, t is the time and $\vec{j_E}$ is the total energy flux density. Thus, ρ_E only changes if there are gradients in the energy flux density, which implies that energy is locally conserved. Now it is assumed that the total energy flux density is equal to the heat flux density

$$\vec{j_E} = \vec{j_q} \tag{2.10}$$

and using Fourier's law it follows that

$$\left(\frac{\partial \rho_E}{\partial t}\right) = \nabla(\lambda \cdot \nabla T). \tag{2.11}$$

To further simplify this equation, it is assumed that the change in energy density is proportional to the change in temperature. This corresponds to assuming a temperature-independent volumetric heat capacity c of the body and is conventionally written as

$$\left(\frac{\partial \rho_E}{\partial T}\right) = \left(\frac{\partial u}{\partial T}\right) = c, \tag{2.12}$$

where u is the inner energy density. To be more precise, a distinction between conditions at constant volume V of the body and constant ambient pressure p would have to be made, since bodies at constant ambient pressure expand and contract thermally.Therefore, volume work is being done which would have to be incorporated in the energy balance. However, the thermal expansion of solids is marginal and hence is being neglected. This implies that a constant mass density of the body under consideration can be assumed and allows to identify the volumetric heat capacity at constant pressure c_p and the volumetric heat capacity at constant volume c_V. Thus, it is

$$c_p = c_V = c. \tag{2.13}$$

Using this simplification the variable ρ_E can be changed to the temperature T via

$$\left(\frac{\partial \rho_E}{\partial t}\right) = \left(\frac{\partial T}{\partial t}\right)\left(\frac{\partial \rho_E}{\partial T}\right) = c\left(\frac{\partial T}{\partial t}\right), \tag{2.14}$$

which yields

$$c\left(\frac{\partial T}{\partial t}\right) = \nabla(\lambda \cdot \nabla T). \tag{2.15}$$

Lastly, λ is assumed to be isotropic and independent of temperature, so that it simply is a non-negative real constant in the equation. The equation then reads

$$c\left(\frac{\partial T}{\partial t}\right) = \lambda \nabla \cdot (\nabla T). \tag{2.16}$$

Using the molar heat capacity c_{mole} instead of the volumetric heat capacity c which are related by

$$c = c_{\text{mole}} \frac{\rho}{M}, \tag{2.17}$$

with the mass density ρ and the molar mass M the equation can then be written as

$$\left(\frac{\partial T}{\partial t}\right) = \left(\frac{\lambda M}{c_{\text{mole}} \rho}\right) \nabla \cdot (\nabla T), \tag{2.18}$$

which is called Heat Equation ([13], p. 148). This equation describes heat conduction under the conditions that

1. λ is constant and isotropic
2. c_{mole} is constant, especially temperature independent
3. thermal expansion is negligible
4. there are no energy sources or sinks (such as absorption of light), which implies the energy flow in the body only occurs via heat conduction.

The smaller the temperature changes under consideration, the better these conditions are met. To completely specify a solution of the heat equation one needs to define boundary and initial value conditions.

The steady-state is reached when $\left(\frac{\partial T}{\partial t}\right) = 0$. In this case, the differential equation for the stationary solution is given by the Laplace Equation

$$\nabla \cdot (\nabla T) = 0. \tag{2.19}$$

2.3.1 Specific one-dimensional solution

This section is based on [14]. We want to examine the dynamics of heat-flow more closely. If we assume that the heat only flows in one direction the Heat Equation reduces to

$$\left(\frac{\partial T}{\partial t}\right) = \left(\frac{\lambda M}{c_{\mathrm{m}}\rho}\right)\left(\frac{\partial^2 T}{\partial x^2}\right), \tag{2.20}$$

which is similar to the one-dimensional Schrödinger equation and can be solved likewise by separation of variables as shown below. We are now interested in a solution of this equation on the set $x \in [0, L]$ with $L > 0$ and for the times $t \in [0, t_{\mathrm{end}}]$. To fully specify the problem we also need to introduce boundary conditions (BC) and initial conditions (IC). We choose the initial conditions to correspond to thermal equilibrium so that we have a uniform temperature T_{init} at $t = 0$ for all $x \in [0, L]$. For the boundary condition we choose $T(x = L, t) = T_{\mathrm{init}}$ and $\left(\frac{\partial T}{\partial x}\right)(x = 0, t) = D$ with $D \in \mathbb{R}, D < 0$. Physically, the boundary conditions state that heat is flowing at a constant rate into the system at $x = 0$ and at $x = L$ the temperature is being held constant. The flow rate out of the system at $x = L$ is not fixed but will change as the system evolves. Therefore, we describe a system that is initially at thermal equilibrium. At $t = 0$ heat starts flowing into the system at a constant rate at $x = 0$ which takes the system out of equilibrium. The dynamics are governed by the one-dimensional Heat Equation.

It is helpful to introduce dimensionless coordinates in order to simplify the equation. For this we transform

$$[0, t_{\mathrm{end}}] \mapsto \left[0, \frac{t_{\mathrm{end}}}{t_0}\right], t \mapsto \tau = \frac{t}{t_0} \tag{2.21}$$

and

$$[0, L] \mapsto [0, 1], x \mapsto \xi = \frac{x}{L} \tag{2.22}$$

so that the equation becomes

$$\frac{1}{t_0}\left(\frac{\partial T}{\partial \tau}\right) - \left(\frac{\lambda M}{c_{\mathrm{m}}\rho L^2}\right)\left(\frac{\partial^2 T}{\partial \xi^2}\right) = 0. \tag{2.23}$$

We can now fix the timescale t_0 by setting

$$\frac{t_0 \lambda M}{c_{\mathrm{m}}\rho L^2} \stackrel{!}{=} 1 \Rightarrow t_0 = \frac{c_{\mathrm{m}}\rho L^2}{\lambda M} \tag{2.24}$$

and introduce a dimensionless temperature via

$$\Gamma = \frac{T}{T_0}, T_0 \in \mathbb{R}, T_0 \neq 0, \tag{2.25}$$

which leaves us with the simplified equation in dimensionless coordinates

$$\left(\frac{\partial \Gamma}{\partial \tau}\right) - \left(\frac{\partial^2 \Gamma}{\partial \xi^2}\right) = 0. \tag{2.26}$$

The boundary and initial conditions are transformed to

$$\begin{aligned} \Gamma(\xi = 1, \tau) &= \frac{T_{\text{init}}}{T_0}, \\ \left(\frac{\partial \Gamma}{\partial \xi}\right)(\xi = 0, \tau) &= \frac{DL}{T_0}, \\ \Gamma(\xi, \tau = 0) &= \frac{T_{\text{init}}}{T_0}. \end{aligned} \tag{2.27}$$

Lastly, we want to formulate the problem in a way that has homogeneous boundary conditions. Therefore, at first calculate the steady-state solution is computed, which is defined by

$$\begin{aligned} \left(\frac{\partial^2 \Gamma_{\text{st}}}{\partial \xi^2}\right) &= 0, \\ \Gamma_{\text{st}}(\xi = 1) &= \frac{T_{\text{init}}}{T_0}, \\ \left(\frac{\partial \Gamma_{\text{st}}}{\partial \xi}\right)(\xi = 0) &= \frac{DL}{T_0}, \end{aligned} \tag{2.28}$$

where Γ_{st} does not depend on τ and hereafter introduce a new variable $v(\xi, \tau)$ as

$$v(\xi, \tau) = \Gamma(\xi, \tau) - \Gamma_{st}(\xi). \tag{2.29}$$

If we substitute this into the Eq. 2.26 and into the initial and boundary conditions 2.28 we finally arrive at a dimensionless equation with homogeneous boundary conditions.

$$\begin{aligned}\left(\frac{\partial v}{\partial \tau}\right) - \left(\frac{\partial^2 v}{\partial \xi^2}\right) &= 0,\\ v(\xi = 1, \tau) &= 0,\\ \left(\frac{\partial v}{\partial \xi}\right)(\xi = 0, \tau) &= 0,\\ v(\xi, \tau = 0) = \frac{T_{\text{init}}}{T_0} &- \Gamma_{st}(\xi).\end{aligned} \tag{2.30}$$

In our specific case the solution of the steady-state is given by

$$\Gamma_{st}(\xi) = \frac{DL}{T_0}(\xi - 1) + \frac{T_{\text{init}}}{T_0}. \tag{2.31}$$

To solve Eq. 2.30 one makes the ansatz

$$v(\xi, \tau) = \phi(\xi)\psi(\tau), \tag{2.32}$$

which implies

$$\psi\left(\frac{\partial^2 \phi}{\partial \xi^2}\right) - \left(\frac{\partial \psi}{\partial \tau}\right)\phi = 0. \tag{2.33}$$

At first, we want to solve the spatial part of this equation. Since ψ and $\left(\frac{\partial \psi}{\partial \tau}\right)$ do not depend on ξ we set $\psi = C_1$ and $\left(\frac{\partial \psi}{\partial \tau}\right) = C_2$ which are now treated as constants with respect to the dependence on ξ. In the case $C_1 = \psi = 0$ we simply reach the trivial solution $v = 0$. Therefore, we set $C_1 \neq 0$ and we introduce

$$\alpha = -\frac{\left(\frac{\partial \psi}{\partial \tau}\right)}{\psi} = -\frac{C_2}{C_1} \tag{2.34}$$

yielding the second order ordinary differential equation

$$\left(\frac{\partial^2 \phi}{\partial \xi^2}\right) + \alpha\phi = 0. \tag{2.35}$$

There are now three different cases for α.

Case 1: $\alpha < 0$

We call $-k^2 = \alpha$ with $k > 0$. The general solution to the differential equation is then given by

$$\phi = A \exp(k\xi) + B \exp(-k\xi) \tag{2.36}$$

with real constants A, B. The boundary conditions from Eq. 2.30 imply $\phi(1) = 0$ since otherwise the time evolution vanishes. This yields $A = -B \exp(-2k)$. Furthermore, we have

$$\left(\frac{\partial \phi}{\partial \xi}\right)(0) = kA - kB = 0 \Rightarrow A = B \tag{2.37}$$

and it follows

$$A = B = 0 \tag{2.38}$$

for $\alpha < 0$, which simply yields the trivial solution which we are not interested in.

Case 2: $\alpha = 0$

In this case we have

$$\left(\frac{\partial^2 \phi}{\partial^2 \xi}\right) = 0 \Rightarrow \phi = A\xi + B, \tag{2.39}$$

with $A, B \in \mathbb{R}$. $\phi(1) = 0$ implies $A = -B$ and

$$\left(\frac{\partial \phi}{\partial \xi}\right)(0) = 0 = A \Rightarrow B = 0, \tag{2.40}$$

which is again the trivial solution.

Case 3: $\alpha > 0$

The general solution in this case is given by

$$\phi(\xi) = A \cos(\sqrt{\alpha}\xi) + B \sin(\sqrt{\alpha}\xi) \tag{2.41}$$

and the boundary conditions yield

$$\left(\frac{\partial\phi}{\partial\xi}\right)(0) = 0 \Rightarrow B = 0 \tag{2.42}$$

and

$$\phi(1) = 0 \Rightarrow A\cos(\sqrt{\alpha}) = 0 \Rightarrow \cos(\sqrt{\alpha}) = 0 \tag{2.43}$$

since we would once again reach the trivial solution. Thus, we find that α can only have the values

$$\alpha = \pi^2\left(n + \frac{1}{2}\right)^2 \qquad n \in \mathbb{N}_0 \tag{2.44}$$

since $\alpha > 0$. We find a discrete but infinite set of solutions to the spatial part given by

$$\phi_n(\xi) = A_n \cos\left(\pi\left(n + \frac{1}{2}\right)\right) \qquad n \in \mathbb{N}_0, \tag{2.45}$$

where $A_n \in \mathbb{R}$. The similarity to the Schrödinger equation is visible here. Due to the linearity of the equation, superpositions of the different solutions are solutions as well. Since α is constant we can now also solve the temporal part by using Eq. 2.34. We find

$$\psi(\tau) = E\exp(-\alpha\tau) \qquad E \in \mathbb{R} \tag{2.46}$$

and because only discrete values for α are allowed we get

$$\psi_n(\tau) = E_n \exp\left(-\pi^2\left(n + \frac{1}{2}\right)^2\tau\right) \qquad n \in \mathbb{N}_0. \tag{2.47}$$

The general solution to Eq. 2.30 is then given by

$$v(\xi,\tau) = \sum_{n=0}^{\infty} B_n \cos\left(\pi\left(n + \frac{1}{2}\right)\xi\right)\exp\left(-\pi^2\left(n + \frac{1}{2}\right)^2\tau\right) \qquad n \in \mathbb{N}_0, B_n \in \mathbb{R}. \tag{2.48}$$

Lastly, we need to determine the coefficients B_n by using the initial condition. It is

$$\int_0^1 \cos\left(\pi\left(n+\frac{1}{2}\right)\right)\cos\left(\pi\left(m+\frac{1}{2}\right)\right)\mathrm{d}\xi = \frac{1}{2}\delta_{nm} \qquad n,m\in\mathbb{R}. \tag{2.49}$$

So, the functions $\cos\left(\pi\left(n+\frac{1}{2}\right)\right)$ are orthogonal to each other with respect to integration over $[0,1]$. Therefore, we can compute the coefficients B_n by

$$\frac{B_n}{2} = \int_0^1 v(\xi,0)\cos\left(\pi\left(n+\frac{1}{2}\right)\xi\right)\mathrm{d}\xi, \tag{2.50}$$

with

$$v(\xi,0) = \sum_{n=0}^{\infty} B_n \cos\left(\pi\left(n+\frac{1}{2}\right)\xi\right). \tag{2.51}$$

The calculation for the initial conditions chosen here can be accomplished by partial integration which yields

$$B_n = \frac{2DL}{T_0\left(\pi\left(n+\frac{1}{2}\right)\right)^2} \qquad n\in\mathbb{N}_0. \tag{2.52}$$

The solution for Γ is then given by

$$\begin{aligned}\Gamma(\xi,\tau) &= v(\xi,\tau)+\Gamma_{st}(\xi)\\ &= \sum_{n=0}^{\infty}\frac{2DL}{T_0\left(\pi\left(n+\frac{1}{2}\right)\right)^2}\cos\left(\pi\left(n+\frac{1}{2}\right)\xi\right)\exp\left(-\pi^2\left(n+\frac{1}{2}\right)^2\tau\right)\\ &\quad+\frac{DL}{T_0}(\xi-1)+\frac{T_{\text{init}}}{T_0}.\end{aligned} \tag{2.53}$$

The solution is a sum of a time-dependent part and a time-independent part given by the steady-state solution. The time evolution is characterized by a series of exponential decays. Higher order terms are suppressed scaling with $\mathcal{O}(n^{-2})$. Since $|\cos(x)|\leq 1, \quad \forall x\in\mathbb{R}$ the summands of the series approach 0 quickly and a good approximation is obtained by only taking the first few terms of the series. Additionally, terms with increasing n decay faster due to the quadratic increase with n in the exponent. Terms with increasing n decay increasingly quickly and only affect the short-term behavior. For example at $\tau = 0.1$ the exponential for

$n = 0$ has decayed to ≈ 0.78 whereas the exponential for $n = 1$ is already at ≈ 0.11. Therefore, the time evolution for times sufficiently large can be well approximated by only the first term. This also means that we can define a 'mean lifetime' by

$$t_{\text{mean}} = t_0 \frac{4}{\pi^2}, \tag{2.54}$$

where the leading order term ($n = 0$) has decayed to $\frac{1}{e} \approx 0.37$ and the second order term is already at $e^{-9} \approx 10^{-4}$. Moreover, at $\tau = 1 \Rightarrow t = t_0$ we have $e^{-\frac{\pi^2}{4}} \approx 0.08$. Recalling that t_0 was chosen in terms of material constants and the length of the system as

$$t_0 = \frac{c_{\text{mole}} \rho L^2}{\lambda M} = \frac{c_{\text{mass}} \rho L^2}{\lambda} = \frac{c L^2}{\lambda}, \tag{2.55}$$

we can estimate the time it takes to reach the steady state by calculating t_0. c_{mass} is the specific heat capacity. In the case of a copper wire at $T = 20\,^{\circ}\text{C}$ with $L = 1\,\text{m}$, $c_{\text{mass}} = 0.386\,\text{J}\,\text{K}^{-1}\,\text{g}^{-1}$, $\rho = 8.93\,\text{g/cm}^3$ and $\lambda = 394\,\text{W}\,\text{K}^{-1}\,\text{m}^{-1}$ [15] we get $t_0 \approx 2.4\,\text{h}$. Materials with larger thermal conductivity λ and smaller volumetric heat capacity $c = c_{\text{mole}}\rho/M$ are faster to reach the steady-state since the heat can flow faster and less heat is stored in the medium. The latter leads to a speed-up of the change of temperature gradients which in turn - following Fourier's law - increases the heat flow and thereby increases the speed to reach the steady state.

The steady-state solution

In general the steady-state solution for the one-dimensional problem is given by solving

$$\left(\frac{\partial^2 \Gamma_{st}}{\partial \xi^2} \right) = 0 \tag{2.56}$$

on a subset of $\mathbb{R}$. The solutions are polynomials of first order given by

$$\Gamma_{st} = a\xi + b \qquad a, b \in \mathbb{R}. \tag{2.57}$$

Specifying the problem by defining boundary conditions fixes a and b. Therefore, the spatial temperature dependence is linear. After Fourier's law this implies that the heat flux density is constant throughout the body which is consistent with the steady state of the continuity equation (Eq. 2.9) since it states that the change of the energy density vanishes. Therefore, at the steady-state there is no net energy

flowing in or out of the system. Instead, the energy is transported through the system governed by Fourier's law. The temperature gradient is the same for all ξ for which the problem is defined and is exactly large enough to give rise to a heat flow corresponding to the heat flowing in and out of the system. Conversely, when the steady-state has not been reached there are changes to the energy-density which means energy is being stored in the system or released from the system.

2.3.2 Cylindrical 3-dimensional Heat Equation with simple boundary conditions

Often, the heat flow through cylindrical bodies such as wires is interesting. The results from the previous section can be generalized if a right cylinder with its symmetry-axis parallel to the x-axis and with constant radius is considered. The bottom base lies at $x = 0$ and the top base at $x = L$. The boundary conditions are given so that there is a constant heat flow through the bottom base, specified by

$$\begin{aligned} \left(\frac{\partial T}{\partial x}\right)(x=0,t) = D \qquad & D \in \mathbb{R}, D < 0, \\ \left(\frac{\partial T}{\partial y}\right)(x=0,t) = 0, & \\ \left(\frac{\partial T}{\partial z}\right)(x=0,t) = 0 & \end{aligned} \tag{2.58}$$

and a constant temperature at the top base given by

$$T(x = L, t) = T_{\text{init}}. \tag{2.59}$$

Furthermore, it is demanded that no heat flows out through the side by setting the normal temperature gradient at the side surface to 0:

$$\nabla T_{\text{at side,normal to side}} = 0. \tag{2.60}$$

In this special case, the solution given in section 2.3.1 is the solution to this 3-dimensional problem since there are no gradients in the y- and z-direction, no heat is flowing through the sides and the boundary conditions are chosen symmetrically. Furthermore, the heat-flow through the bottom base specified by the boundary condition at the bottom base and by Fourier's law is equally distributed across the bottom base. In this case the heat flux density is given by

$$|\vec{j_q}| = \frac{P}{A}, \tag{2.61}$$

with P being the amount of heat flow at the bottom base and A the area of the bottom base. In the following, A is called the cross-section. As explained in the previous section, at steady-state conditions the heat flow through the system is spatially and temporally constant. Therefore, Fourier's law can be used to relate cross-section A, heat-flow P, length L, the total temperature difference $\Delta T = |T(x = 0) - T(x = L)|$ and thermal conductivity λ at steady-state conditions:

$$|\vec{j_q}| = \frac{P}{A} = \lambda |\frac{\partial T}{\partial x}| = \lambda \frac{\Delta T}{L}. \tag{2.62}$$

The total temperature difference ΔT is the difference of the temperature at $x = 0$ and the temperature at $x = L$. Here, the temperature dependence of the thermal conductivity λ has been neglected. Eq. 2.62 allows to calculate the temperature difference for a body with constant cross-section A across its length L given the heat-flow through the body at steady state conditions. However, this equation is only valid under the assumption that the body is straight and has no curvature along the symmetry axis and that the heat flowing in or out is equally distributed across the cross-section. Of course, this kind of argument can be extended to other geometries such as cuboids, as long as the body's cross-section is translation-invariant parallel to the heat flow. If these conditions are violated, the one-dimensional solution cannot be extended to the 3-dimensional problem so easily since the gradients are not restricted to one dimension anymore. In this case finding an analytical solution is much more difficult since a partial differential equation has to be solved on a 3-dimensional manifold with boundary conditions on 2-dimensional manifolds. However, Eq. 2.62 will be used nonetheless in the following to design the cooling system under the assumption that it is still a good approximation for curved geometries and non-uniformly distributed heat flux densities.
Remarkably, for steady-state conditions the only relevant material-specific parameter is the thermal conductivity λ. Good heat conductors (materials with large λ) show smaller temperature differences across their length compared to bad heat conductors given that the heat flux densities are equal. This can be thought of as a temperature difference 'needed' to give rise to heat flow. Alternatively, one can also think of a temperature 'resistance' $L/(\lambda A)$. Then, Eq. 2.62 is similar to Ohm's law for electricity in a wire where P corresponds to the electrical current I and ΔT corresponds to the electrical potential difference $\Delta\phi$ or voltage U across the wire. By contrast, the volumetric heat capacity c does not influence the steady-state, since when the steady state is reached the energy density does not change anymore. Instead, the heat capacity influences the time it takes to reach the steady state.

2.4 Thermal contact conductance

Two solid bodies seemingly in contact, microscopically actually only touch at a few points [16]. Heat conduction is thereby limited to those touching spots. The heat flow is constricted to narrow channels which increases the heat flux density and after Fourier's law the temperature difference across the interface. Since the thickness of the connection is usually of the order of µm and thus thin compared to the dimensions of the bodies itself this appears as a sharp temperature drop between the bodies [16]. To quantify this phenomenon one introduces the thermal contact conductance

$$h = \frac{P_{\text{heat flux}}}{A\Delta T}, \tag{2.63}$$

where $P_{\text{heat flux}}$ is the heat flux through the interface, A is the apparent touching surface of the bodies and ΔT is the sharp temperature drop across the interface. The larger thermal contact conductance the smaller is the temperature drop across the interface. The reciprocal of h is called thermal contact resistance [16].
In addition to heat transfer by conduction through the touching spots there can be heat conduction through the medium filling the gaps between the bodies or by radiation across the gap. Radiation can be neglected unless the temperature drop is large. Due to the usually small thickness of the gap convection can generally be neglected. Therefore, there remain two contributions contact conductance. The conduction through touching points of the interface is called solid spot conductance whereas the conduction through interstitial medium is called gap conductance. For vacuum conditions gap conductance can only occur if one introduces an interstitial medium [16].

2.4.1 Solid spot conductance

The solid spot conductance depends on many factors such as contact pressure, thermal conductivity, surface roughness, hardness and mean slope of the surface profile. Empirically, the dependence of solid spot conductance on the pressure p follows a power law

$$h_{\text{solid spot}} = \alpha p^{\beta}, \tag{2.64}$$

with $\alpha > 0$ and $\beta \in [0.66, 0.95]$[16]. To compute the solid spot conductance detailed information about the surface state as well as the contact pressure needs to be taken into account. These factors are not always known and therefore the solid spot conductance is often a principal uncertainty for heat transport processes. To give an idea of the order of magnitude, the solid spot conductance for aluminum

alloy and stainless steel with a center line average roughness of 1 µm for both and a slope of both surfaces of 0.18 rad with a pressure of 0.1 MPa is 626 $W/(m^2K)$[16]. For the same parameters and a pressure of 0.5 MPa the solid spot conductance is 2842 $W/(m^2K)$.

2.4.2 Gap conductance

At low contact pressures and in the presence of interstitial material, the heat transfer takes place primarily through the gap. If a gas fills the gap the ratio of gap thickness to mean free path of the gas has to considered since the efficiency of energy transfer of a single collision is low. For low pressures and rough surfaces the gap conductance through the gas is reduced. Because the thermal conductivity of a gas is independent of its pressure above a threshold pressure, the gas gap conductivity is constant. The threshold is reached when the mean free path is of the order of the gap thickness. At pressures below 130 Pa, the gas conductance can be neglected compared to the solid spot conductance [16].
On the other hand, if a liquid is the interstitial material, the surface tension needs to be taken into account. Liquids with low surface tension entirely wet the surfaces and therefore fill the gap completely. In this case, the thermal contact conduction can be calculated by simply dividing the thermal conductivity by the mean gap thickness. This holds for most liquids, for example water. In the case of high surface tension such as liquid metals the gap is not filled completely. Subsequently, a reduced contact area has to be calculated and afterwards the contact conductance has to be inferred [16].

2.4.3 Bolted Joints

When bolting two plates together the actual contact area of the plates is limited to a circular area around the bolt hole. The contact pressure decreases in the radial direction from a maximum at the bolt hole to almost zero within a short distance. As a consequence, the heat flow through a bolted connection is concentrated to the area around the bolted hole. This area is called 'contact zone' in the following. As explained above, at the contact zone the two surfaces also only touch at a few points. Therefore, we have a 'macroscopic' constriction by the bolted connection in addition to the 'microscopic' constriction as discussed above [16].
The contact conductance increases with rising torque due to the grow of pressure at the interface. Moreover, the contact conductance for bolted joints increases with the radius of the contact zone since the effective area is larger. However, the pressure distribution at the bolted connection affects the contact conductance only weakly . Instead, the total mechanical load is decisive. The contact conductance also depends on the bolt hole radius, the thickness of the plates and the surface

roughness as well as properties of the materials such as elasticity. All in all, this causes the computation of bolted joints to be difficult and beyond the scope of this work. Unfortunately, the empirical data for bolted joints is also sparse. Hence, in practice one is often restricted to knowing the qualitative influences when trying to control thermal contact conductance of bolted joints [16].

3 Resistance thermometers

The electrical resistance of most materials is temperature dependent. This allows construction of thermometers if the dependency is well known. Such thermometers are called resistance thermometers, thermistors or resistance temperature detectors (RTD). They are manufactured from different materials such as metals, semiconductors or ceramic. For some of those there are standardized values of the resistance and its temperature dependence.
To perform a temperature measurement with these sensors requires measuring the electrical resistance. In principle, the resistance can be determined by any technique capable of measuring electrical resistances such as a Wheatstone Bridge or a simultaneous measurement of voltage and current [17]. In practice however, often the so-called '2-wire' or '4-wire' circuits and variation of those are chosen.

3.1 2-wire and 4-wire circuits and variants

The 2-wire circuit for resistance measurement consists of a constant current source and a voltmeter. This is shown in Fig. 3.1. The resistance can then be calculated by Ohm's law. This arrangement is problematic in the case that the wires connecting the RTD to the evaluation unit are long. In this case the wires' resistances distort the measurement. If the lengths of the wires and the specific electrical resistance are well known this can be corrected for. Alternatively, one can use the 4-wire circuit to cope with wire resistances.

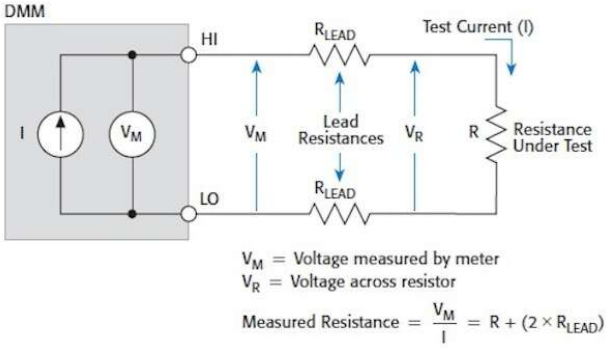

Figure 3.1: 2-wire setup with a constant current source and digital multimeter [18].

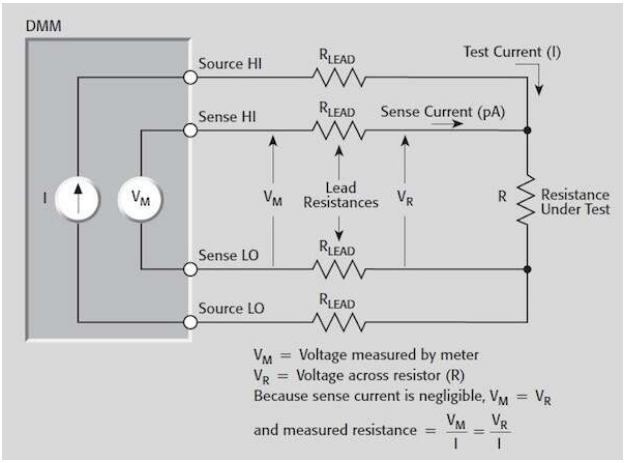

Figure 3.2: 4-wire setup with a constant current source and digital multimeter [19].

The 4-wire circuit introduces two additional wires to the 2-wire circuit as depicted in Fig. 3.2. The constant current source is connected via the so called 'force' wires to the resistor. The voltmeter is wired to the resistor parallel to the constant current source and these wires are called 'sense' wires. The idea is to reduce the current through the wires connecting the voltmeter and the RTD but not through the RTD itself. Since voltmeters have large internal resistances the current through the sense wires is small by design. After Ohm's law, the voltage across the sense wires is then reduced, whereas the voltage across the RTD is the same as for the 2-wire circuit since this is supplied by the current source in parallel. Therefore, the wires' resistances can be neglected compared to the RTD resistance.
Instead of measuring the current and voltage simultaneously, the setup can also be modified by using a reference resistor whose resistance is accurately known. In this

case, the reference resistor and RTD are wired in series and a voltage is applied to the circuit which realizes a voltage divider circuit. The voltage across the RTD and across the reference resistor are then measured. By Kirchhoff's circuit laws the resistance of the temperature sensor can then be determined. This has the benefit that the current does not have to be known. Instead, two voltages are being measured. A drawback is that the accuracy is limited by the reference resistor. This modification can be applied to both 2- and 4-wire arrangements.

3.2 Self-heating

By applying a voltage across the RTD, a current flows through it. This causes heat to be dissipated in the resistor. The rate of dissipation is given by

$$P_{\text{heat dissipation}} = U \cdot I = R_{\text{T}} I^2, \tag{3.1}$$

where I is the electrical current. Due to this current, the resistor heats up which is called self-heating. This effect is a systematic error in the measurement of temperature. The heat dissipated in the resistor will be emitted to the environment. The better this heat transfer is, the lower the systematic heating of the resistance. To minimize self-heating, it is important to use low currents. However, the currents and voltages cannot be chosen arbitrarily small since the sensitivity of the measurement devices such as voltmeters and ampere-meters has to be respected. Moreover, for very low currents effects like thermal noise in the circuit could distort the signal.
Self-heating is particularly challenging in the case of temperature measurement in vacuum conditions. In this case, there is no medium in contact with the probe other than the body whose temperature should be measured. As a consequence, the dissipated heat can be released only by radiation, conduction to the attached body or conduction through the measurement wires. Therefore, when measuring temperature, the body whose temperature is to be determined, is actually heated. This is of course also true for non-vacuum conditions but the heat can then be emitted to the surrounding gas or liquid and heating of the measurement point is thereby reduced.
Self-heating depends strongly on the operating conditions. Manufacturers of resistance temperature detectors often specify self-heating coefficients E for specific conditions so that the error by self-heating can be calculated as

$$\Delta t = I^2 R_{\text{T}} E. \tag{3.2}$$

With Eq. 3.2 the increase in temperature in K can be calculated. The coefficients E are given in $\mathrm{K\,mW^{-1}}$ [20]. Typical values are $0.2\,\mathrm{K\,mW^{-1}}$ for air with an average speed of $2\,\mathrm{m\,s^{-1}}$ and $0.02\,\mathrm{K\,mW^{-1}}$ for water at a speed of $0.2\,\mathrm{m\,s^{-1}}$ [20].

3.3 Platinum resistance thermometers

A common material for use as a thermometer is platinum due to its reliability and reproducible electrical properties [21]. The characteristics of a platinum thermometer are standardized (IEC 751). For the temperature range of $0 - 850\,°\mathrm{C}$ the resistance dependency is well described by a second order polynomial as

$$R_\mathrm{T}(\theta) = R_0 \left(1 + A\theta + B\theta^2\right), \tag{3.3}$$

where θ is the temperature in °C, R_0 is the resistance at $0\,°\mathrm{C}$, $A = 3.9083 \times 10^{-3}\,°\mathrm{C}^{-1}$ and $B = -5.775 \times 10^{-7}\,°\mathrm{C}^{-2}$ [21]. The value of R_0 is used to characterize a sensor. For example, a device with $R_0 = 100.00\,\Omega$ is called 'Pt100'.
The standard defines different tolerance classes for platinum resistance sensors. Class A's temperature deviation is limited to

$$\Delta\theta_A = \pm\left(0.15\,°\mathrm{C} + 0.002|\theta|\right), \tag{3.4}$$

whereas class B's is given by

$$\Delta\theta_B = \pm\left(0.30\,°\mathrm{C} + 0.005|\theta|\right). \tag{3.5}$$

The best accuracy of these standardized probes is therefore given at $0\,°\mathrm{C}$.

4 Experimental setup: Frequency comb and high-harmonic generation

Fig. 4.1 shows the setup of the laser system. A commercial frequency comb system is used as the initial light source (MenloSystems FC1000-250, [22]), with an average power of 10 W, a repetition rate of 100 MHz, a carrier wavelength of 1035 nm and a pulse width of 24 ps. Afterwards, the laser pulses are amplified in an Yb-doped rod-type fiber amplifier to 80 W average power. Subsequently, the pulses are temporally compressed with a grating compressor to reach pulse lengths of 200 fs.

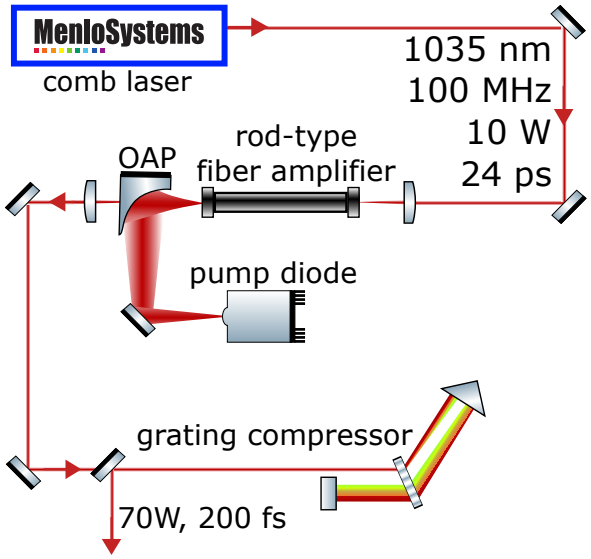

Figure 4.1: Experimental setup of the laser system [23].

The laser pulses are guided into an ultra-high vacuum (UHV) chamber where consecutive pulses are overlapped inside an enhancement cavity and high-harmonics are generated. A simplified sectional schematic of the vacuum chamber is depicted in Fig. 4.2. The optical elements are mounted on a titanium structure which is

directly connected to the optical table. On the contrary, the vacuum chamber is floating on air-lifted feet so that no mechanical vibrations of the chamber, for example from the vacuum pumps, are transfered to the optical elements. The whole laser table additionally rests on pneumatic vibration isolators [24].

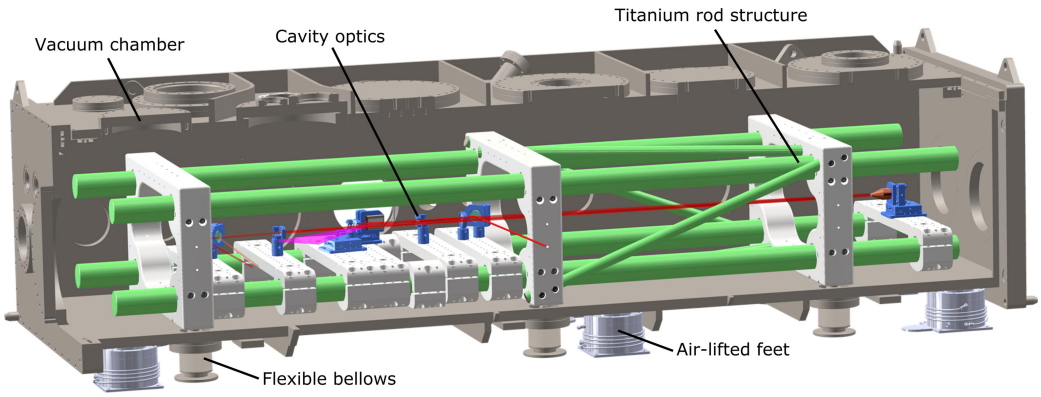

Figure 4.2: Sectional view of vacuum chamber with laser cavity inside [25].

To reach high peak intensities needed for high-harmonic generation, an enhancement cavity is used, where the length of the cavity is controlled so that the consecutive pulses interfere constructively. The repetition rate is 100 MHz, so that the length of one round-trip needs to be 3 m. The enhancement cavity consists of five mirrors which are all located in the UHV chamber. A top view of the interior of the vacuum chamber is shown in Fig. 4.3. One mirror serves as in-coupling (IC) mirror. Additionally, there are four high-reflectivity mirrors. Two of them are spherical concave ('Curved mirror 1 and 2') and in another one there is a diffraction grating with 2000 lines/mm etched into the surface ('Grating-mirror'). The fourth of the high reflecting mirrors is used to control the length of the cavity. To accomplish this, the Pound-Drever-Hall-technique is applied [26]. The mirror is moved by a piezo-crystal to lock the laser cavity length and ensure constructive interference. Therefore, we call this mirror 'Piezo-mirror' in the following. It is glued to a tungsten carbide block.

The laser light enters the cavity through the In-coupling mirror. Afterwards, the beam is focused and reflected from Curved mirror 1 to the Grating-mirror and from there to Curved mirror 2. To complete the round-trip, the beam is guided to the Piezo-mirror and lastly revisits the In-coupling mirror. HHG takes place at the focus between both curved mirrors, where the peak light intensity and thus the electric field amplitude is maximal. There, a noble gas is injected through a nozzle. The generated XUV-light propagates collinearly with the initial pulses and is diffracted at the Grating-mirror due to its smaller wavelength whereas the

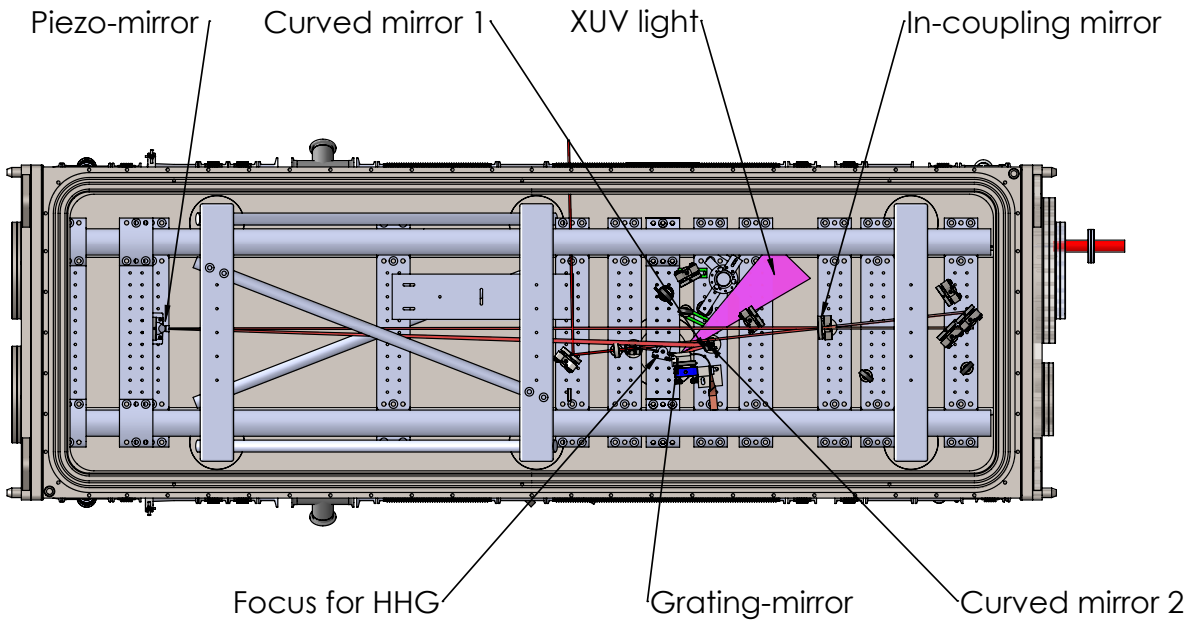

Figure 4.3: Top view of the enhancement cavity inside the UHV chamber.

infrared laser light is reflected in zeroth order. The XUV-light leaves the cavity and is intended for precise spectroscopic measurements of HCI in a trap (Cryogenic Paul Trap Experiment at the Max-Planck-Institute for Nuclear physics). To facilitate this, long term and high stability operation of the XUV comb is essential.
To remove the injected noble gas from the chamber, a differential pump system enclosing the gas nozzle is installed so that the injected gas through the nozzle is quickly removed from the UHV chamber. This is shown in Fig. 4.4. The pump system consists of three different stages. There is a turbopump for each stage, effectively removing the injected gas and preventing plasma effects. The differential pump system can be lifted to allow for changes in the experimental apparatus.

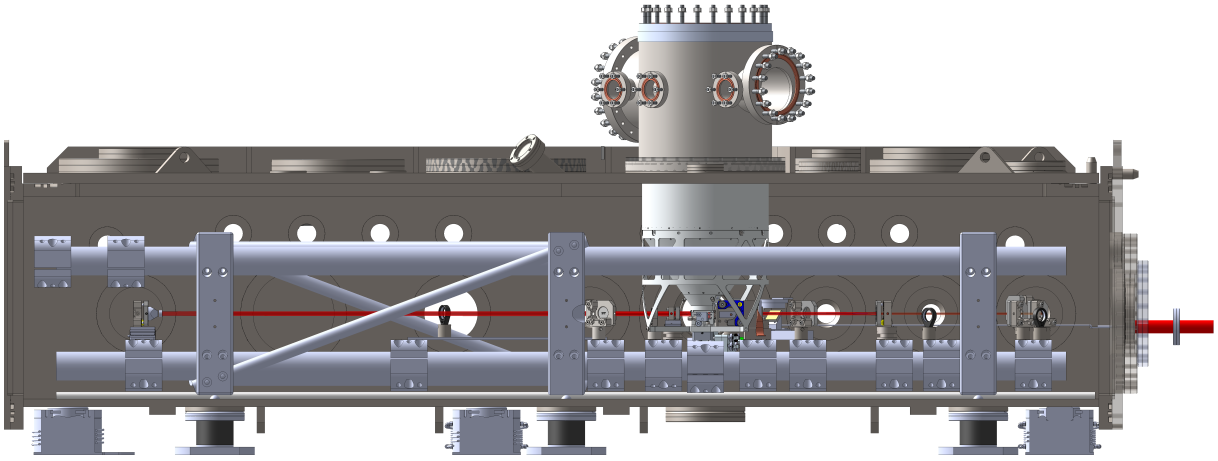

Figure 4.4: Side view cut of the UHV chamber showing the differential pump system.

5 Design of cooling system

5.1 Design considerations and requirements

The total heat load P_{tot} that needs to be removed from the mirrors is not known. Therefore, a conservative estimation based on the total cavity losses is made and the cooling system is overdesigned. This allows to cope with uncertainties in the calculation methods and unknown thermal contact resistance (see Section 2.4). Furthermore, by overdesigning the possibility to scale up the laser power in the future is provided. The cavity losses are estimated to 1 W, which corresponds to approximately 1% at full laser power. Additionally, it is assumed that these losses are distributed equally over all five cavity mirrors that need to be cooled. Thus, $P = 0.2\,\text{W}$ per mirror in the dimensioning of the cooling system is used.
Moreover, the system has to be UHV-compatible, which constrains the suitable materials, it may not impair the performance of the cavity and it should be easily implemented. For example, the pump system should still be liftable without having to dismantle parts of the cooling system. Crucially, the system may not transfer vibrations to any optical elements because this impedes the cavity. Moreover, one wants the system to be general in the sense that the concept can be extended to other devices in the chamber and the existing setup should not be heavily modified. Ideally, the system also should provide the opportunity to adjust the temperature without having to modify the setup. Most importantly, the concept should be able to restrict the temperature increase of the mirrors during operation of the cavity significantly compared to the increase without cooling system and thereby improve the performance of the cavity. This should enable continuous long-term operation of the cavity under controlled and stable conditions.

The setup is operated in vacuum conditions which eliminates the possibility to cool by convection. Cooling the devices directly by radiation requires a large surface to be attached to the mirrors and does not allow for control without significant modification to the experimental setup. Therefore, we choose to cool the components by conduction. As mentioned in Sec. 2.3, the typical timescales for the dynamics of heat conduction over a length of 1 m are of the order of hours. Since the objective is to have a continuously operating frequency comb we restrict our design considerations to the steady-state and use Eq. 2.62 as our tool for calculation. To keep the temperature increase as small as possible, we need a thermal reservoir with a temperature lower than the temperature of the devices. In order to decrease

the temperature of the mirrors we then could use a low reservoir temperature or decrease the temperature difference itself by controlling the parameters L and A. However, it could be detrimental to provide a heat reservoir with a temperature much lower than room temperature. In this case, if the cavity is non-operational we might have unwanted thermal compression of the mirrors since they are cooled lower than room temperature. Alternatively or additionally, the alignment might be impaired. Therefore, we choose to plan with a heat reservoir with a temperature close to room temperature but leaving the option open to decrease the temperature further if needed and possible after installation of the cooling system.
Due to that, we need to make sure the temperature differences ΔT are small. Eq. 2.62 then requires the cross-sections A to be large, the lengths L to be small and the thermal conductivity λ to be large. Heuristically, we aim to constrain the temperature differences to $\approx 1\,\mathrm{K}$. As heat conducting material we choose copper due to its large thermal conductivity, its availability UHV compatibility.

5.2 Description of the cooling system

Fig. 5.1 shows a schematic overview of the cooling system exemplarily for one of the curved mirrors.

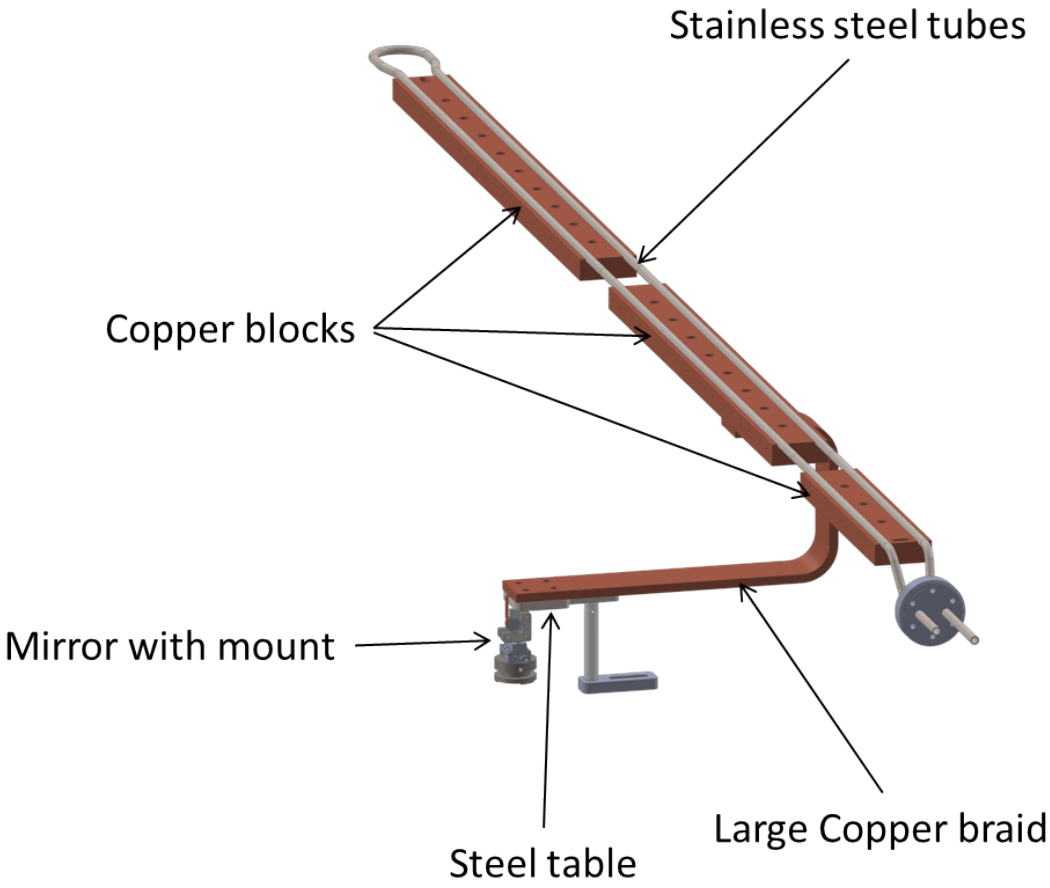

Figure 5.1: Schematic overview of the cooling system. The external air cooled water chiller is not shown.

The cooling system consists of a cooling water cycle including a temperature controlled, air-cooled water chiller [27], copper blocks, a flexible copper braid with large cross-section per mirror, thin copper foil, a smaller copper braid and fixture tables. The water chiller is not shown in Fig. 5.1. The cooling water flows through stainless steel tubes within the vacuum chamber, which are thermally connected to the copper blocks. The latter serve as thermal reservoirs whose temperature

will be held approximately constant by the cooling water. The flexible copper braids are thermally connected to the copper blocks and are fixed on tables next to the respective mirror. Using either thin copper foil or a smaller copper braid, the mirrors are thermally connected to the large copper braid. This arrangement allows the heat to flow from the mirrors through the foil or small braid to the large braids and from there to the copper blocks. There, the heat is distributed throughout the material and ultimately removed from the chamber by the cooling water. Lastly, the air cooled water chiller emits the heat to air outside the cleanroom and thereby regulates the water temperature to an adjustable fixed temperature.

5.2.1 Description of important single components

Fig. 5.2 and 5.3 show one of the designed copper blocks. The copper blocks are manufactured from oxygen-free high-conductivity copper. Two semicircular parallel indentations are milled in the surface to insert the stainless steel tubes. A small slit is located at the bottom of the semicircular indentation for the soldering process. At the lower side there are multiple sets of 4 quadratically arranged threaded holes where the large copper braids can be screwed to. The threaded holes are vented by small bores at the sides. Additionally, there are multiple clearance holes between the sets of threaded holes to allow for attachment of devices later on. Elongated holes are added so that struts can be bolted to the copper blocks to support the structure. The lengths of the three blocks are chosen so that the distance between titanium structure and cooling system is sufficient to make sure the cooling system does not touch the titanium structure and thereby transfer vibrations. Moreover, the lengths of the blocks are not allowed to exceed $\approx 0.8\,\mathrm{m}$ due to the manufacturing process (described further below).

The large copper braids are made of electro copper due to availability considerations. Fig. 5.4 shows one of the braids. They consist of many small wires which are pressed without soldering into solid copper husks at both sides under high pressure. The manufacturer claims to guarantee low contact resistance between husk and wires [28]. The braids are flexible and thus isolate the optical elements from vibrations due to the waterflow through the tubes which is crucial in order to achieve stability of the optical cavity. There are 4 quadratically arranged clearance holes on each husk to bolt the braids to the fixture tables and to the bottom of the copper blocks.

The fixture table surfaces are stainless-steel plates that are shaped to match the husks of the large copper braids to screw the braid-husk to the table. Additionally, there is an elongated hole beyond the connection surface which is used to attach the table to a post. This is shown in Fig. 5.5.

Despite relatively low thermal conductivity, stainless steel is used as a material for water transport. This was chosen to prevent corrosion and therefore ensure the

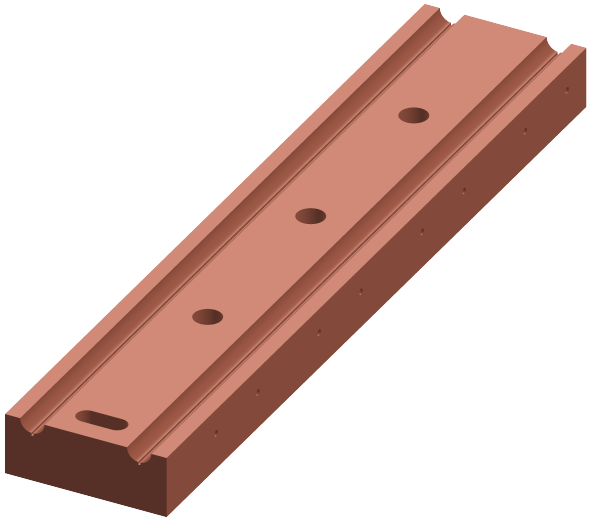

Figure 5.2: Tilted view of the top of the shortest copper block.

tightness of the water tubes. Moreover, stainless steel is mechanically stable and can hold part of the construction's weight.

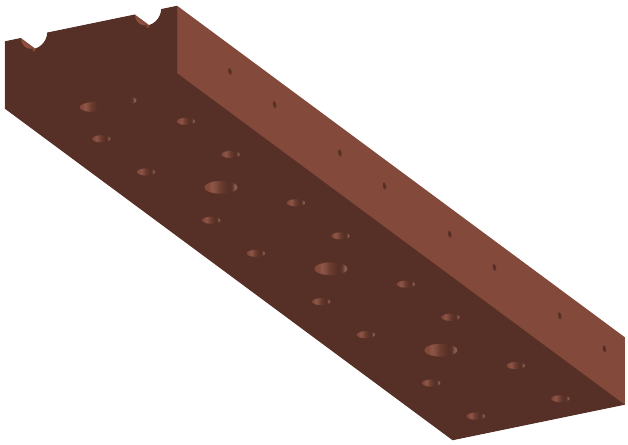

Figure 5.3: Tilted view of the bottom of the shortest copper block showing the quadratically arranged threaded holes on the bottom.

Figure 5.4: Large copper braid manufactured from electro copper with a cross-section of 210 mm^2 [28].

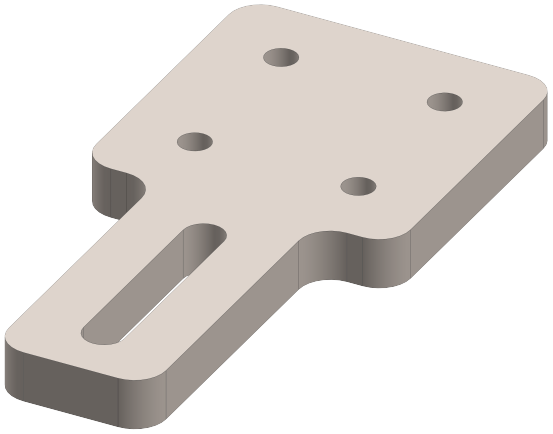

Figure 5.5: Tilted view of a steel desk showing the elongated hole where the desk can be affixed on a post as well as the four holes to screw the braid-husk to.

5.2.2 Assembly and manufacturing of the cooling system

Fig. 5.6 and 5.7 show detailed exemplary views of the assembly of mirror, foil, large braid and steel table.

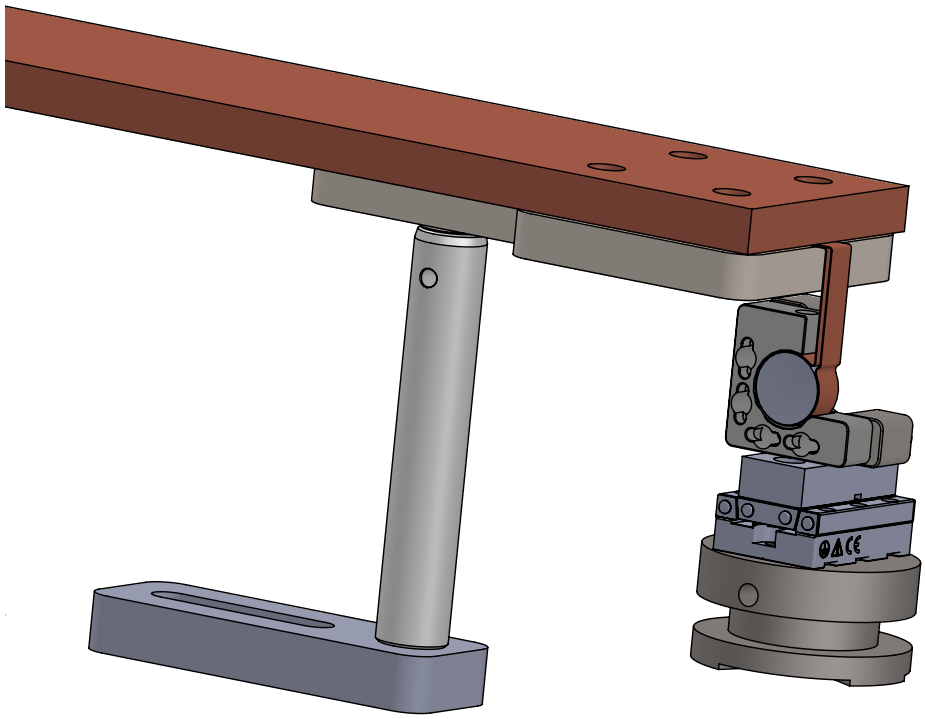

Figure 5.6: Tilted view of the thermal connection between mirror, foil and large copper braid.

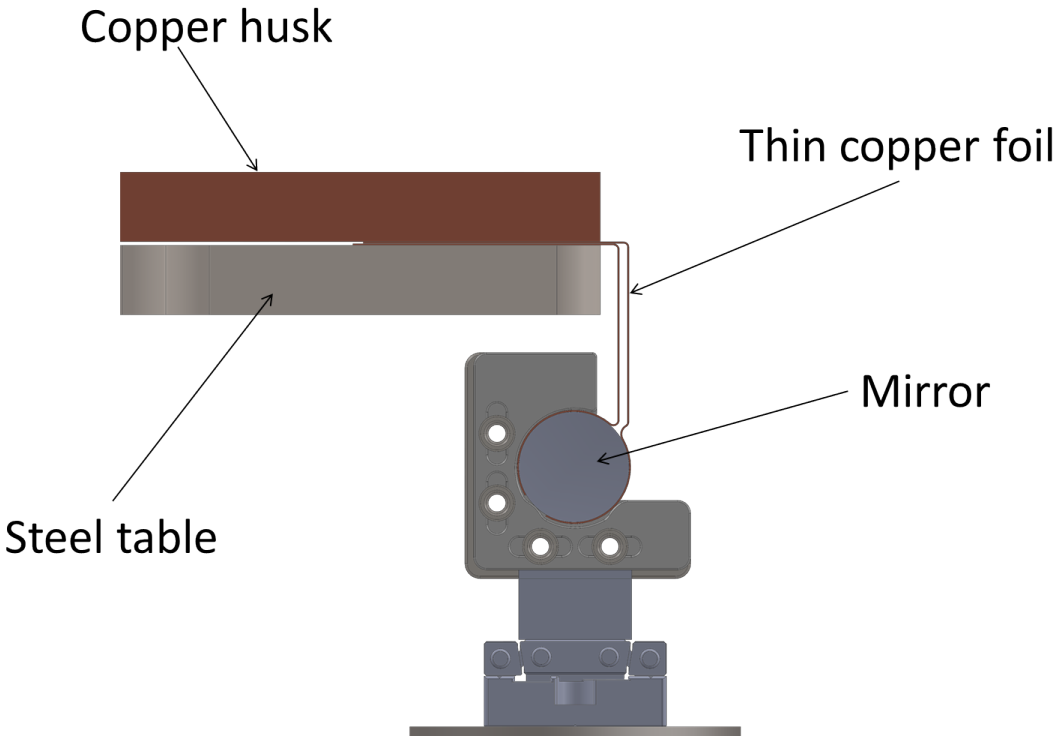

Figure 5.7: Detailed view of the thermal connection between mirror, thin foil and large copper braid.

Stainless steel tubes and copper blocks are hard-soldered in a vacuum soldering furnace whose length is limited to $\approx 1\,\mathrm{m}$. This also constrains the lengths of the tube parts and forces to weld the different tube parts together after the soldering process so that 3 different parts are welded together after soldering each copper block to stainless steel tubes. The hard solder used is a mixture of silver and copper which are good heat conductors and allow heat transfer between tubes and copper blocks. The assembly of copper blocks and steel tubes is shown in Fig. 5.8.

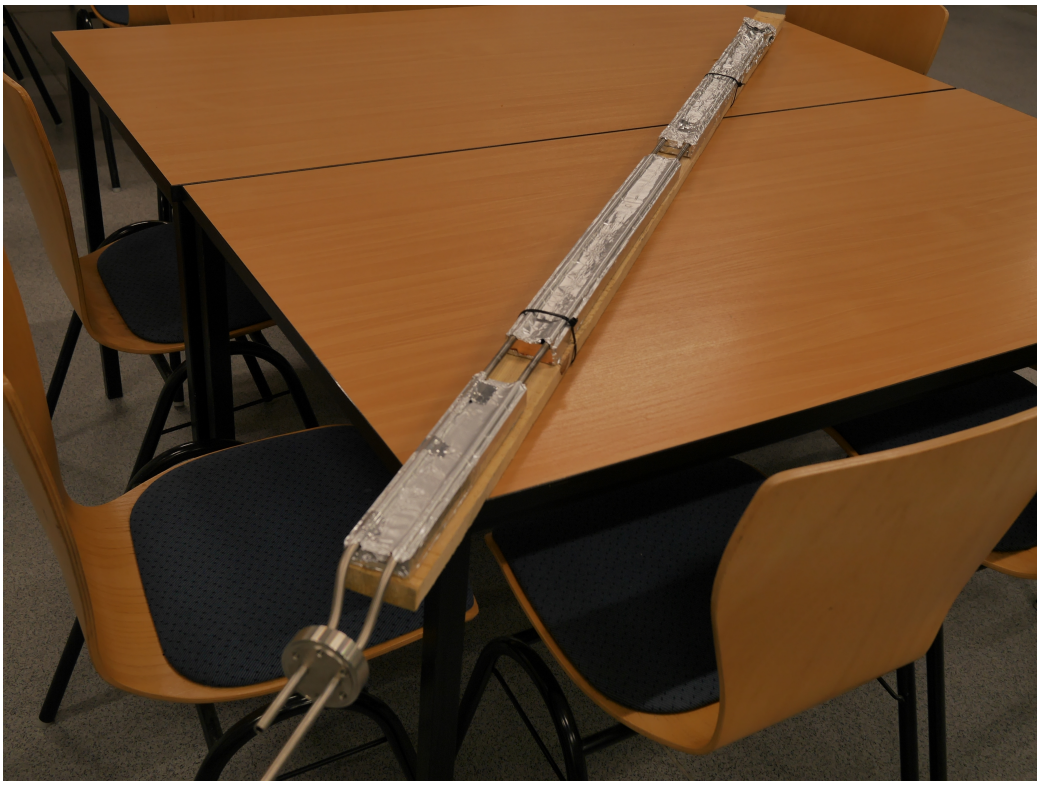

Figure 5.8: Copper blocks, steel tubes and modified CF50 flange after soldering tubes to blocks and welding tubes together. The assembly is mounted on a piece of wood to avoid transportation damage.

The construction of tubes and copper blocks is positioned above the titanium structure in the vacuum chamber so that it does not impair the operation of the frequency comb and does not block access to the chamber. Additionally, this position saves space in the chamber for optical elements in the future. To decouple vibrations of the copper blocks and tubes from the titanium structure the blocks are supported on aluminum struts which stand on the chamber floor. Fig. 5.9 and 5.10 show the positions of the cooling system in the UHV chamber and of the steel tables. The stainless steel tubes are bent at the beginning to increase the vertical distance between titanium and cooling system.

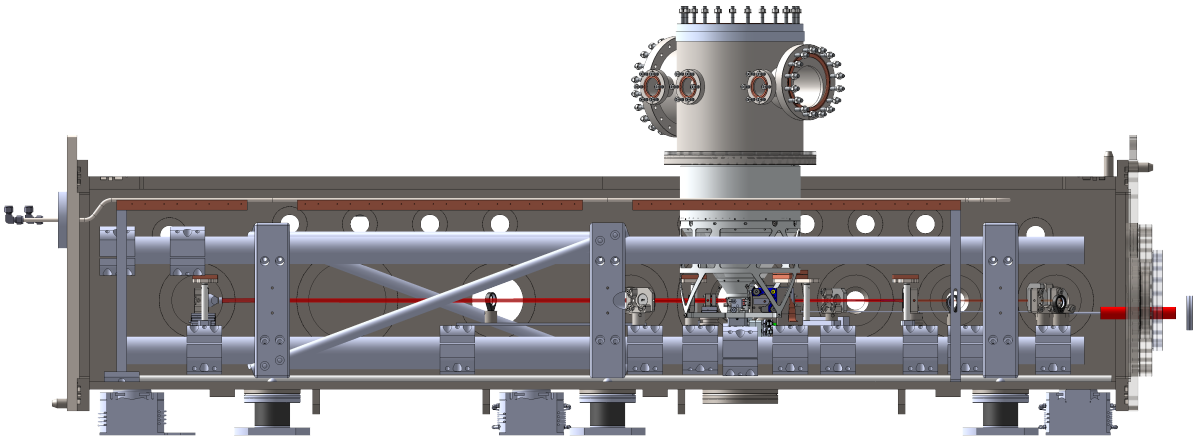

Figure 5.9: Side view cut of the UHV chamber with cooling system, steel tables and copper husks of the large braids. The braids themselves are not shown in order increase clarity.

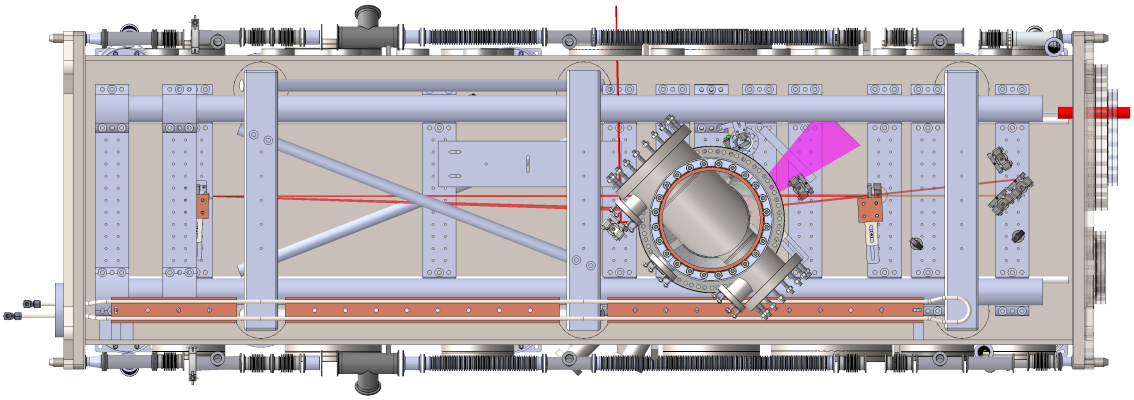

Figure 5.10: Top view cut of the UHV chamber with cooling system, steel tables and copper husks of the large braids. The braids themselves are not shown in order increase clarity.

The large braids are screwed to the copper blocks and to the fixture tables so that the thin foil is clamped between steel table and husk of the large copper braid.

5.2.3 Thermal connections between mirrors and large braids

Since the connection between large braid and mirror is unique for each mirror this will be described separately in the following paragraphs.

Piezo-mirror Because the piezo-mirror is oscillating against the tungsten carbide we choose not to attach the cooling foil directly to the mirror itself to avoid impairment of the cavity-lock. Instead, the copper foil is glued to the circular side surface of the tungsten carbide body using a vacuum compatible epoxy resin [29]. The loose end of the foil is led to one of the fixture tables where it is clamped between husk of one of the large copper braids and the table by bolting the husk to the table. The table is positioned in order to reduce the distance between glued connection and large copper braid.

Curved mirror 1 This mirror is positioned close to the differential pump system. To still allow for the possibility to easily lift the pump system the fixture table cannot be stationed at the close side to the copper blocks, so it is placed on a post on the far side from the mirror and protrudes from there to the mirror. Copper foil is glued to the side surface of the mirror. The foil is cut to match the thickness of the mirror. The foil's loose end then is led to the fixture table where it is clamped between table and husk of the large braid as described above. The braid also is guided in order to allow for easy lifting of the pump system.

Grating-mirror and Curved mirror 2 There is not enough space to use a fixture table for both of these elements so we use one table for both instead, which we position between the two devices. Similar to curved mirror 1 we glue copper foil to the sides of curved mirror 2 and lead the loose end to the fixture table where it is clamped between husk and table. However, since there is already a small copper braid glued to the grating-mirror we use this instead of copper foil. The small braid is guided to the fixture table as well. In contrast to the other connections it is not clamped between table and husk of braid but instead clamped between husks of two braids, so that we obtain a 'sandwich' structure. The order of elements in the 'sandwich' from bottom to top then is steel-table, copper foil from curved mirror 2, husk of braid 1, small braid, husk of braid 2. This structure is held together by bolts.

In-coupling mirror The mount of this mirror differs from the curved mirrors. Therefore, the copper foil has to be twisted to be led to the fixture table after being glued to the side surface of the mirror. Aside from this the foil, large braid and table assembly is as described for the piezo-mirror.

5.2.4 Reducing thermal contact resistance

To enhance heat flow via the bolted connections and mitigate thermal contact resistance (cf. 2.4) a thin film of vacuum grease [30] is introduced onto the connecting surface before bolting. This increases the effective contact area between the heat conducting surfaces so that heat flow can occur through the thin film of grease where microscopically the bodies are not in contact. This technique is used for the bolted connection of copper block to large braids as well as for the connection of thin foil and small braid to large braid. Additionally, we tighten the screws of the connections firmly to increase the contact pressure and contact area. The contact resistance between copper foil and mirrors or tungsten carbide cannot be reduced by increasing the pressure due to the mirrors being affixed to the mirror mounts. As described above this connection is glued instead, so that the glue increases the effective thermal contact between foil and mirror or tungsten carbide respectively.

5.2.5 Vacuum-tight water feed-through

The water feed-through has to satisfy the requirement that the lid of the vacuum chamber, where the feed-through is localized, still needs to be removable after installation of the cooling system. Therefore, a double-flange system is employed which is depicted in Fig. 5.11. The tubes carrying water are welded to holes in a modified CF50 flange. The CF50 flange has threaded holes situated within the CF50 cutting edge. This flange is then bolted to a modified CF63-flange which has a hole in its middle where the water tubes are sticking through. The CF63-flange is bolted to the lid on a CF63 weld flange. To remove the lid after installation one has to first loosen all screws of the CF63-flange and remove it. The modified CF50-flange and the water tubes are then not attached to the lid anymore so the lid can be removed while the cooling system stays in the chamber.

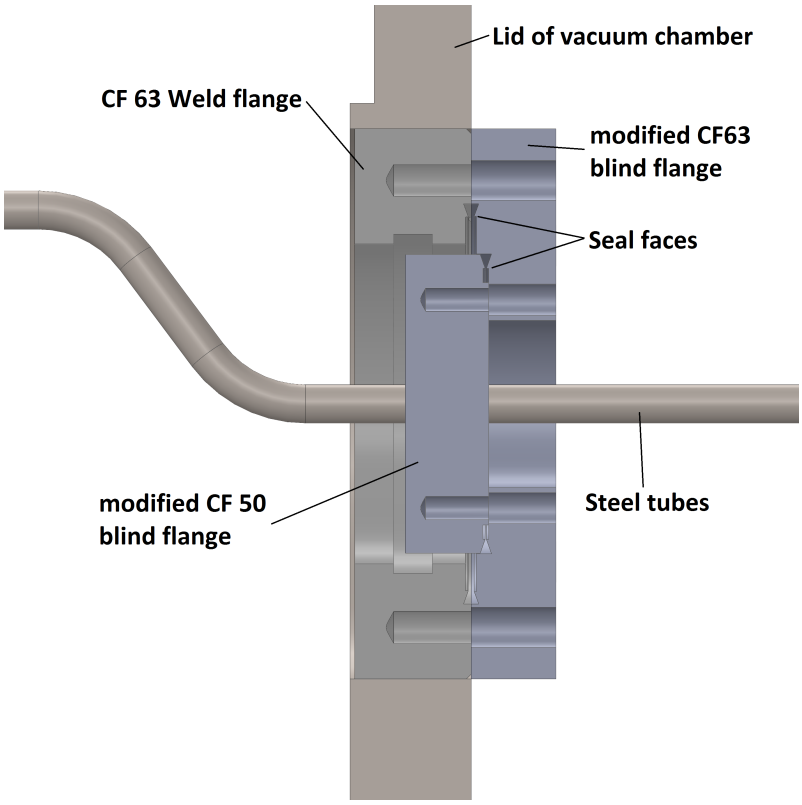

Figure 5.11: Side view cut through the vacuum-tight water feedthrough assembly showing bolted connections. Copper gaskets are not shown.

5.3 Expected temperature differences

Eq. 2.62 is used to estimate the temperature differences across the large copper braid, the small copper braid and across the copper foil under the assumption that each conducts $P = 0.2\,\mathrm{W}$ at steady-state conditions. The length of the braid is measured to be $L = (40 \pm 4)\,\mathrm{cm}$ and the cross-section is $A = 210\,\mathrm{mm}^2$. We use a value of $\lambda = (380 \pm 10)\,\mathrm{W/(Km)}$ [15]. This gives an expected temperature difference across the large copper braids of $\Delta T = (1.00 \pm 0.10)\,\mathrm{K}$.
For the small copper braid it is estimated that $L = (7 \pm 2)\,\mathrm{cm}$. The small braid has a cross-section of $A = 10\,\mathrm{mm}^2$ which yields a temperature difference of $\Delta T = (3.7 \pm 1.1)\,\mathrm{K}$.
To estimate the temperature difference for the copper foil a distinction is made between single-layer and double-layer foil. Furthermore, it is assumed that the foil is 0.2 mm thick and 6.37 mm wide which corresponds to the thickness of the mirrors. Then, the temperature differences for $L_{\mathrm{min}} = 10\,\mathrm{mm}$ and $L_{\mathrm{max}} = 50\,\mathrm{mm}$

are given by

$$\begin{aligned} \Delta T_{\text{single-layer,L}_{\text{min}}} &= 4\,\text{K} \\ \Delta T_{\text{single-layer,L}_{\text{max}}} &= 20\,\text{K} \\ \Delta T_{\text{double-layer,L}_{\text{min}}} &= 2\,\text{K} \\ \Delta T_{\text{double-layer,L}_{\text{max}}} &= 10\,\text{K} \end{aligned} \tag{5.1}$$

These values, as well as the values for the small copper braid, illustrate that it is crucial to minimize the distance between mirror and large copper braid to succeed in cooling the mirrors. However, it is clear that the heuristically chosen design goal to restrict the temperature difference to 1 K will not be satisfied. Instead, the total temperature difference from mirror to copper block is expected to be in the range $3 - 11\,\text{K}$ assuming double-layer foil. Of course, this holds only if the heat load is 0.2 mW which is an overestimation. In reality, smaller dissipated heat is expected and therefore the temperature differences will also be smaller. The maximum permitted temperature of the mirrors is not specified by the manufacturer, but according to an oral request, a continuous operation temperature of the mirrors in the range of 300-400 °C is tolerable. These bounds will easily be fulfilled with the cooling system.

6 Preliminary heating measurements

To investigate heating of the mirrors due to absorption of laser radiation, a measurement in a small test vacuum chamber is set up. A metallic mirror instead of a dielectric mirror is used to enhance the temperature increase since metallic mirrors generally show higher absorption. Therefore, the laser power can be greatly reduced as well. An aluminum half-inch mirror (Thorlabs, PF05-03-F01) is used, which has a reflectance of $\approx 90\,\%$ at the carrier wavelength of the laser (1035 nm) [31]. Therefore, the mirror absorbs $\approx 10\,\%$ of the incident laser power. The test chamber allows easier positioning of mirror and laser light than the large UHV chamber so that the measurement setup is simplified.

6.1 Setup of the test measurement

The test chamber setup is shown in Fig. 6.1. The chamber is cylindrical and at the top there is a large window. Additionally, there are 8 smaller ports available arranged circularly around the chamber. A turbopump is mounted at one of these and connected to a prevacuum pump. In another port there is a pressure detector and the wires for the temperature measurement are fed through yet another port (cf. Sec. 6.2). The laser light is guided through a window in one of the remaining ports and reflected from the mirror in the chamber. The beam is then sent to a power meter detecting the reflected power of the beam. Lastly, there is another window consisting of Zinc selenide (ZnSe), flange-mounted at one of the ports. This allows for the observation of the mirror with an infrared thermo camera (FLIR InfraCam, spectral region: 7.5-13 µm) since this material has a high transmissivity for these spectral regions. The mirror is positioned in the middle of the cylindrical chamber and is mounted on a high stability mirror mount comparable to the actual cavity mirror mounts. The temperature sensor is glued to the backside of the mirror (cf. Sec. 6.2).

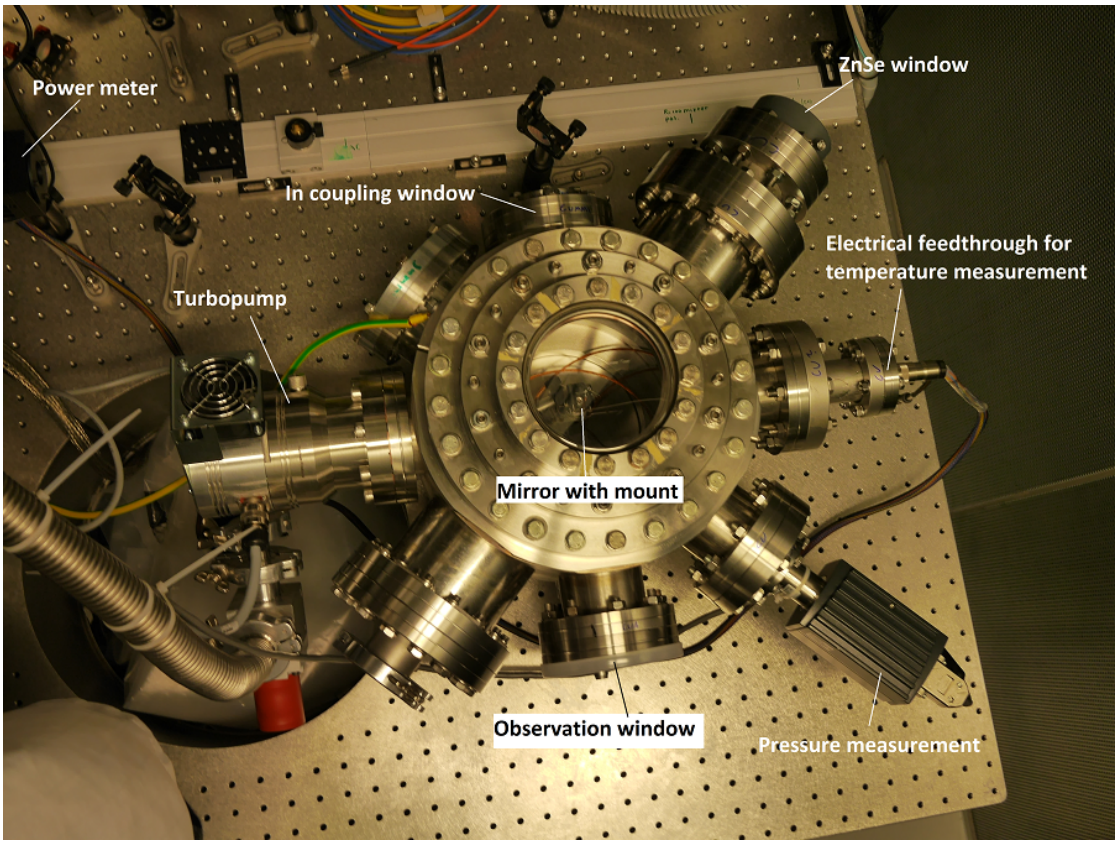

Figure 6.1: Picture of the test chamber setup. The mirror is positioned at the center of the chamber.

6.2 Setup of temperature measurement

Pt1000 resistance temperature detectors (RTD) are used to measure the temperature. Chip sensors are employed ([32], PCA 1.2010.10S, length 10 mm, tolerance class A) which consist of a platinum layer sputtered onto a ceramic substrate. Due to the low volume of the sensor it has a fast response time to changes in the temperature. An image of the sensors used is depicted in Fig. 6.2.

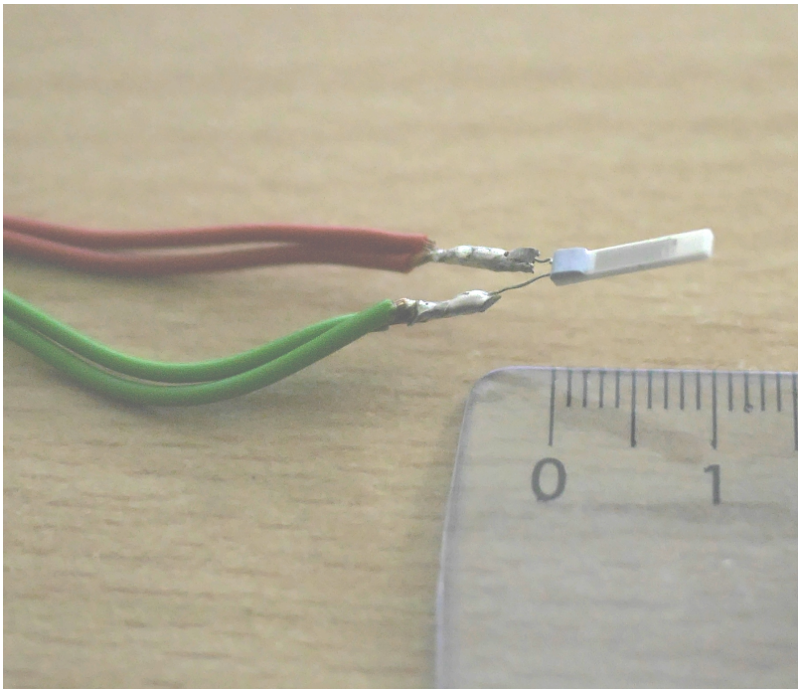

Figure 6.2: Picture of the chip Pt1000 sensor soldered to be used in a 4-wire circuit.

To read out the sensor, a 4-wire circuit is employed since the wires are long and the wire resistances would distort the measurement for a 2-wire circuit [17]. As described in Section 3.1, a reference resistor and voltage measurements are used to determine the temperature-dependent resistance. The ratio of the voltage across the RTD to the voltage across the reference resistor is measured by a fully differential analog-to-digital converter (ADC) and then represented as an integer number. A commercially available integrated circuit, designed specifically for this purpose, is used [33]. The ADC of the chip has a resolution of 15 bits and requires the reference resistor to be greater than the RTD's resistance. The chip is integrated on a printed circuit board, where the peripheral wiring of the chip is arranged according to the specifications of the chip [33]. The assembly of the chip with complementary

components such as the reference resistor on the printed circuit board is called breakout board. The breakout boards which are used here are also commercially available [34]. To operate and interface the breakout boards, we use a commercial microcontroller (Arduino MKRZero, [35]) which communicates with the boards after master/slave procedure via serial peripheral interface. The data is then read from the master and logged digitally.
The RTD's resistance can be calculated as

$$R_{\mathrm{T}} = \frac{z}{2^{15}} R_{\mathrm{ref}}, \tag{6.1}$$

where R_{T} is the temperature dependent resistance, $z \in 0, 1, 2, ..., 2^{15}$ is the output of the ADC and R_{ref} is the reference resistance. The bias voltage applied to the circuit is $V_{\mathrm{bias}} = 2\,\mathrm{V}$ and we use a reference resistor of $R_{\mathrm{ref}} = 4.3\,\mathrm{k\Omega}$ with a tolerance of 0.05 % [36]. There is a maximum current of 0.4 mA through the resistors, where we assumed that the temperature of the RTD is larger than 0 °C so that the total resistance is greater than 5.3 kΩ. This is smaller than the specified maximum current for the RTD of 1 mA [32]. The dissipated heat in the temperature-dependent resistor is therefore $P_{\text{dissipated heat}} \approx 1.2\,\mathrm{k\Omega} \cdot 0.4\,\mathrm{mA}^2 = 0.2\,\mathrm{mW}$. However, the readout-chip offers the possibility to turn off the bias voltage between taking data. Thus, the effective self-heating can be reduced further by only applying the voltage for a short while when data is taken.
For intra-vacuum measurements, the detectors are glued to the measurement site using a low vapor pressure epoxy resin [29] and connected to an electrical feedthrough flange using Kapton-insulated wires [37, 38]. The feedthrough offers 19 pins, so that one can connect maximally 4 probes in 4-wire configuration to the feedthrough. The air-side of the electrical feedthrough is wired to the breakout boards to read out the resistances and thus the temperatures. For measurements outside of vacuum conditions the probes are wired directly to the breakout boards. Microcontroller and breakout boards are assembled in a box which is shown in Fig. 6.3. The box was produced by the on-site electronics workshop at the institute. This setup can be used to readout any Pt1000 sensor connected via 4 wires.

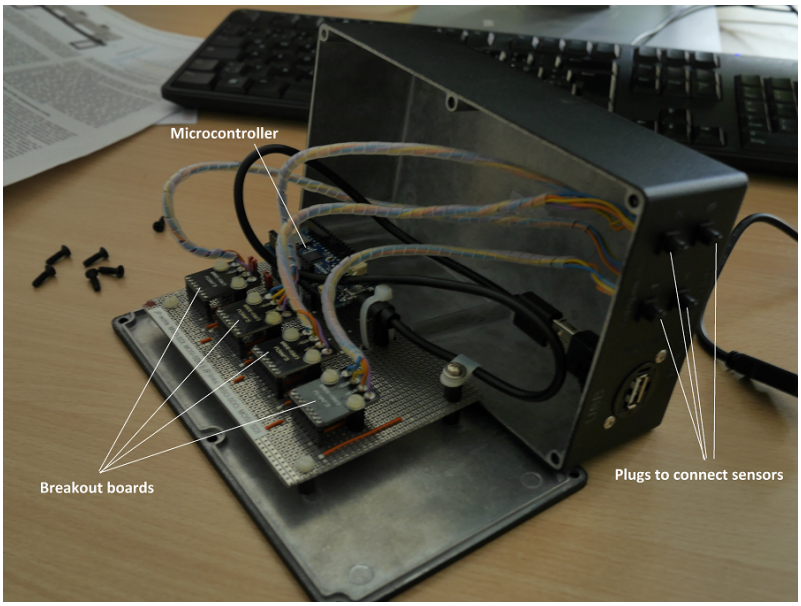

Figure 6.3: Image of the evaluation unit containing a microcontroller and breakout boards. Sensors can be plugged in to measure the temperature in 4-wire configuration. The communication with the microcontroller is facilitated via USB.

6.3 Measurement procedure

Before recording the heating curves, the absorption of the mirror was estimated. To do so, a power meter was inserted at three different positions in the laser path at a low constant laser power. Thus, the power was measured directly in front of the mirror inside the chamber and after the (anti-reflection coated) window , directly behind the window after reflection from the mirror and in front of the window outside of the chamber. No significant absorption of the window itself and an approximate absorption of 10 % of the mirror was found. This value is estimated to be accurate within 2-3 %.
The heating for different laser intensities and pressures in the chamber was measured. One measurement series was conducted at full turbopump power and therefore at high-vacuum conditions. These measurements were performed while the pressure was still decreasing in the chamber, albeit slowly. The first measurement series therefore corresponds to a range of pressures. This approach is justified since it is expected that convection at high vacuum is negligible and a change in pressure therefore does not distort the measurement. The pressure during the first measurement series decreased from a starting value of 3.6×10^{-5} mbar to 6.3×10^{-6} mbar. A second measurement series was performed at ambient pressure.

For both measurement series the same laser powers have been chosen to ensure comparability of vacuum and ambient pressure conditions. The laser powers were determined outside of the chamber after reflection from the mirror with the power meter. The incident intensities were therefore higher. The measured laser powers are shown in Table 6.1.

Table 6.1: Laser powers measured after reflection from the mirror.

No.	laser power vacuum [mW]	laser power ambient pressure [mW]
1	155 ± 3	154 ± 5
2	533 ± 3	541 ± 5
3	794 ± 5	810 ± 7

After reaching thermal equilibrium indicated by constant temperature of the mirror, the laser beam was unblocked and the temperature was recorded until a new steady-state was reached. Afterwards, the beam was blocked again and the system was undisturbed until thermal equilibrium was reached again. Then, the procedure was repeated for different laser intensities. Additionally, at maximum and minimum temperatures, pictures were taken with the infrared-camera to observe the extent of thermal radiation emitted by the components.

6.4 Results and data analysis

6.4.1 Error analysis of temperature measurement

The total absolute errors of the temperature measurement as well as the errors of temperature differences are determined as worst case errors, thus effectively overestimating the errors. There are mainly 4 different sources for deviations of the temperature from the true value. First of all, the resistance temperature detector has a maximum deviation given by Eq. 3.4. Unfortunately, the systematic shift described by this equation is dependent on the specific sensor and may be positive or negative for different temperatures [39]. To decrease the uncertainty introduced by this, a calibration of each sensor would have been necessary.
The fourth error source is due to self-heating of the detector as described in Sec. 3.2. To counteract this effect, the bias voltage for measuring the resistance was only turned on when data was taken and turned off immediately afterwards. Subsequently, the evaluation software paused for 1 s before enabling the bias voltage again and recording another data point. The average time the bias voltage was turned on was $\approx 200\,\mathrm{ms}$ and the average down-time was $\approx 1.4\,\mathrm{s}$. With the maximum heating rate of $0.2\,\mathrm{mW}$ (cf. Sec. 6.2) the effective average heating rate is then given by $\approx 30\,\mu\mathrm{W}$ and we thus neglect the error from this source due to its insignificance.

In addition to this shift, we also have a systematic error due to the reference resistor (cf. 6.2) and due to the analog-to-digital converter (ADC) incorporated on the breakout board. The ADC's errors are threefold. There is an offset error of maximally ±3 least significant bits (LSB), a full-scale error of ±1 LSB determining the difference of the ADC's readout at full input voltage and integral non-linearity (INL) of ±1 LSB specifying the maximum deviation from the ideal linear transfer function [40]. Therefore, the maximum total absolute deviation of the code generated by the ADC is 4 LSB which is the maximum divergence of the actual transfer function from the ideal transfer function given in Eq. 6.1. This cannot exceed 4 LSB since the shift due to offset and full-scale error is bounded by the offset error. In the worst scenario one has to add the INL to this value. The maximum shifted value of the RTD's resistance is then given by

$$R_{\mathrm{T,max.\ shift}} = \frac{(z+\Delta z)(R_{\mathrm{ref}}+\Delta R_{\mathrm{ref}})}{2^{15}} = \frac{zR_{\mathrm{ref}} + z\Delta R_{\mathrm{ref}} + \Delta z R_{\mathrm{ref}}}{2^{15}}, \tag{6.2}$$

where we neglected the term with $\Delta z \Delta R_{\mathrm{ref}}$ due its relative insignificance. Δz is the maximum deviation of the ADC as described above.
To compute the absolute maximum temperature errors, we first calculate the value of the RTD's resistance given by Eq. 3.3, find the associated value of z and determine the maximum shift of the RTD's resistance with the equation above. Inverting Eq. 3.3 and adding the error of the probe (Eq. 3.4), the maximum shifted value of the temperature and the absolute worst case error can be determined. Since z increases with growing temperature, the absolute error also increases with temperature, albeit gradually. At $\theta = 22\,^{\circ}\mathrm{C}$ we find $\Delta\theta_{\mathrm{max}} = 0.47\,^{\circ}\mathrm{C}$ whereas at $\theta = 80\,^{\circ}\mathrm{C}$ it is $\Delta\theta_{\mathrm{max}} = 0.62\,^{\circ}\mathrm{C}$. Remarkably, the three aforementioned errors (ADC, reference resistor and detector) all have the same order of magnitude at room temperature.
To calculate the error of temperature differences for a single sensor it is important to note that the constant shift of the reference resistor's resistance cancels out. This is also true for the offset error of the ADC. Instead, one has to consider the error of the slope of the transfer function of the ADC, called gain error. The gain error is the difference of the full-scale error and the offset error [40]. Therefore, the maximum gain error for the ADC used here is 4 LSB. Additionally, the INL adds an error of 2 LSB in the worst case sceanario. The ideal transfer function is given by Eq. 6.1 whereas the real transfer function can be written as

$$z_{\mathrm{r}} = m_{\mathrm{real}} R_{\mathrm{T}} \pm b, \tag{6.3}$$

with a different slope m_{real} than for the ideal value $m_{\mathrm{ideal}} = 2^{15}/R_{\mathrm{ref}}$. The maximum deviation of differences due to the gain error follows as

$$\begin{aligned}\Delta\Delta z_{\text{gain}} &= |m_{\text{ideal}}|(R_{T,1} - R_{T,2})| - m_{\text{real}}|(R_{T,1} - R_{T,2})|| \\ &= |(R_{T,1} - R_{T,2})| \cdot \left| \frac{2^{15}}{R_{\text{ref}}} - \frac{2^{15} - 4}{R_{\text{ref}}} \right| \\ &= |(R_{T,1} - R_{T,2})| \frac{4}{R_{\text{ref}}}.\end{aligned} \tag{6.4}$$

This depends on the actual difference in the RTD's resistances and is always smaller than 4 LSB. To account for INL a value of 2 LSB has to be added to this. Therefore, the error of differences of RTD's resistances is given as

$$\begin{aligned}\Delta|R_{T,1} - R_{T,2}| &= \frac{|R_{T,1} - R_{T,2}| \, \frac{4}{R_{\text{ref}}} + 2}{2^{15}} R_{\text{ref}} \\ &= \frac{|R_{T,1} - R_{T,2}| \cdot 4}{2^{15}} + 2^{-14} R_{\text{ref}}.\end{aligned} \tag{6.5}$$

When the difference of RTD's resistances at two different data points is much smaller than the reference resistor's resistance, the first summand is negligible. This is the case for all temperature differences in the present measurements so that we can neglect the first term. The error of uncertainties due to the evaluation unit is then determined only by the integral non-linearity (INL). In this case the error due to the ADC and the reference resistor is below 0.1 °C for temperature differences smaller than 100 °C.
As mentioned above, the deviation of the RTD itself is non-uniform and non-monotone over the temperature range [39]. Overcautiously, we thus assume again the unrealistic worst case in which the maximum error due to the probe itself is given by

$$\Delta\Delta\theta_{\text{probe, worst case}} = (0.3\,^{\circ}\text{C} + 0.002\,(|\theta_1| + |\theta_2|)). \tag{6.6}$$

Realistically, the value is expected to be much lower since the deviation from the standardized curve of these sensors does not usually change as drastically as investigated in [39]. Instead, for the temperature range of 0 °C to 50 °C a monotonic, roughly linear increase or decrease is observed limited to less than 10 Ω per 50 °C. With this, the temperature difference error due to the probe is then less than 0.2 °C for a temperature difference of 50 °C. To make use of this and improve the error estimation we assume that the deviation is indeed linear with temperature, but with a larger absolute slope than 10 Ω per 50 °C to account for non-linearities. The improved estimation is illustrated in Fig. 6.4. We assume that the maximum error drift function coincides with the value of the class-A-tolerances at $\theta = 0\,^{\circ}\text{C}$ and $\theta = 50\,^{\circ}\text{C}$ since we know that the sensor's deviations are bounded by these

values. Comparing this to the results presented in [39] we find that this is in fact a conservative approach and one can expect the errors of differences in practice to be even lower.

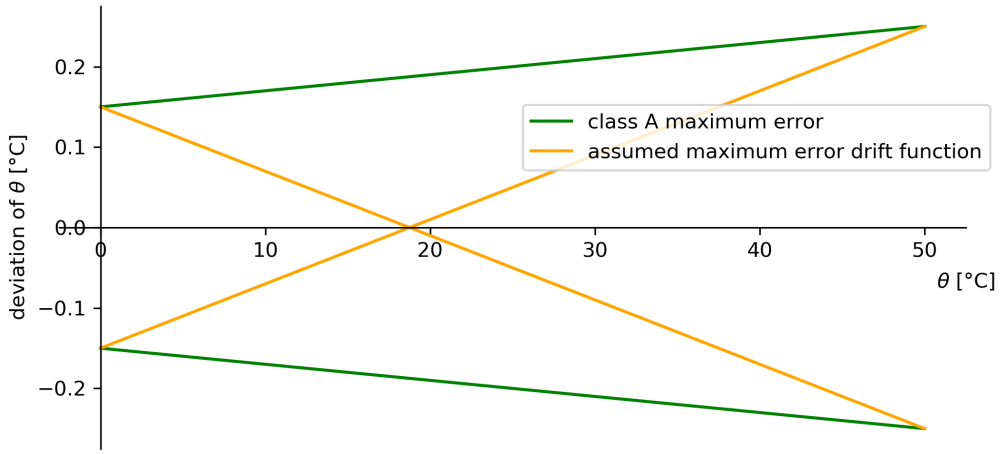

Figure 6.4: Illustration of error estimation for temperature differences. It is assumed, that the deviation scales linearly with temperature and that the slope is in the worst cases given by the limits of the class A tolerance (green curves).

The error of temperature differences due to the probe under this assumption is then given by

$$\begin{aligned} \Delta\Delta\theta_{\text{probe, linear scaling}} &= |\theta_1 - \theta_2| \, \frac{0.4}{50} \\ &= \frac{|\theta_1 - \theta_2|}{125} \end{aligned} \tag{6.7}$$

and grows linearly with the difference itself. In the following we will use this estimation to determine difference errors.

6.4.2 Results

Fig. 6.5 shows the heating curve taken at vacuum conditions. The maximum total error is shown, as elucidated above. Before the second and third measurement, we see smaller peaks where the laser power was adjusted for the next measurement. The dip during the last measurement occurred because the laser beam was blocked accidentally for a short while.

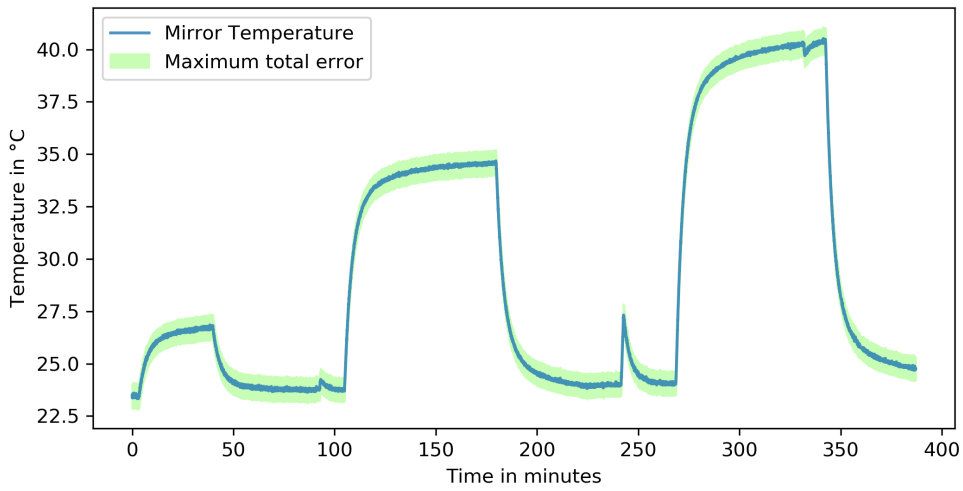

Figure 6.5: Heat curve for vacuum conditions and three different laser powers. The error is the absolute maximum error.

To calculate temperature differences between the steady-states of a cold mirror (no incident laser light) and a hot mirror (incident laser light) at first a constant function is fit to the data before the laser hits the mirror and when the cold steady-state was reached. For this fit the absolute maximum errors as deviations are used. In Fig. 6.6 this is shown exemplarily for the second largest laser intensity at vacuum conditions. The fit-range is restricted to a few minutes before unblocking the beam.

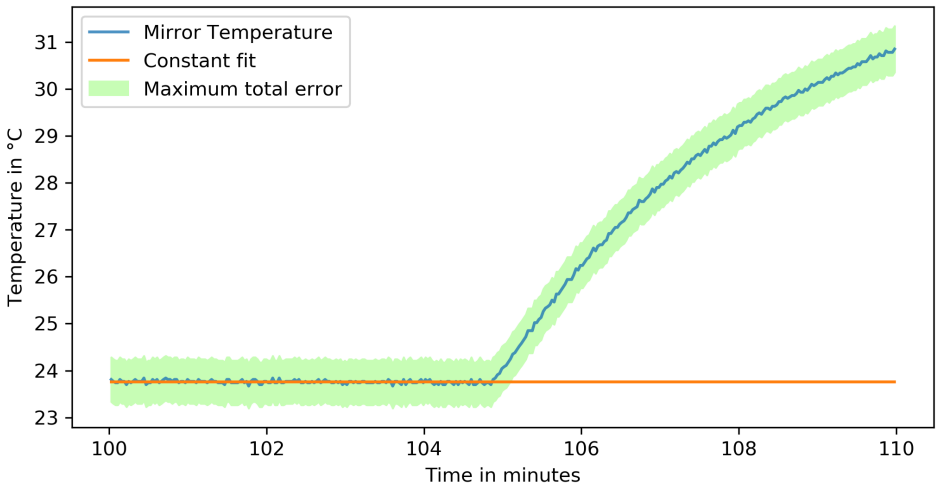

Figure 6.6: Heat curve excerpt for the second biggest laser intensity at vacuum conditions showing the constant fit to determine the initial temperature.

Afterwards, a function of the form

$$f(t) = T_{\text{end}} \left(1 - \exp\left(-\frac{(t - t_{\text{start}})}{\tau}\right)\right) \tag{6.8}$$

is fitted to the increasing temperature data. t_{start} is a start-time for the increase and τ determines the speed to reach the steady-state. Since the steady-state temperature T_{end} is the main interest, values close to the steady-state are used and fast dynamics at the beginning after unblocking the beam are neglected. This is shown in Fig. 6.7.

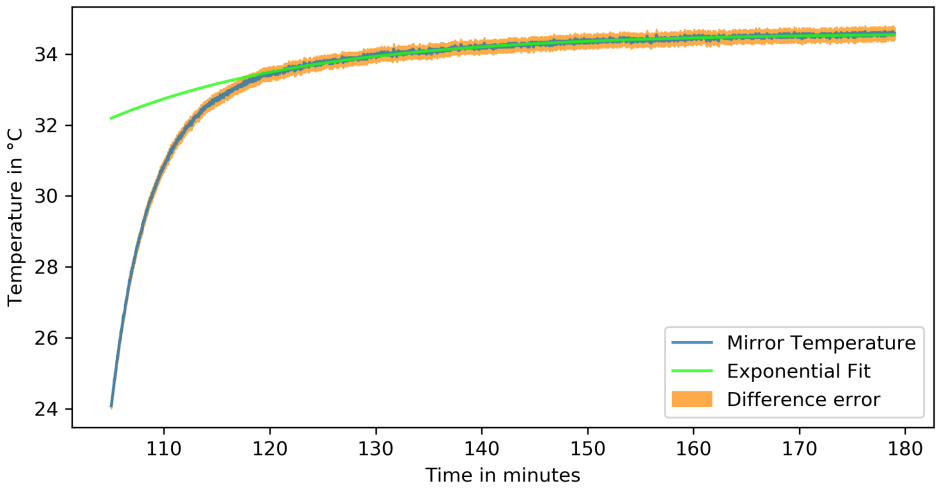

Figure 6.7: Heat curve excerpt for the second biggest laser intensity at vacuum conditions showing the exponential fit to determine the hot steady-state temperature, while neglecting the fast dynamics at the beginning.

Contrary to the constant fit, the difference error with reference to the previously determined initial temperature is now used as deviations for fitting. This is shown in Fig. 6.7 as orange envelope and does not represent the absolute error of the temperatures but the deviation from the initial value. As shown, the fitted curve does not reproduce the fast increase of temperature at the beginning. This indicates that the time response is not simply an exponentially decaying function. However, for longer times after unblocking the beam the fit matches the data almost perfectly, so that this model is justified to be used for determining the steady-state temperature. The results of our analysis are summarized in Table 6.2.

Table 6.2: Steady-state temperature differences for vacuum and ambient pressure conditions and different reflected powers.

	Ref. power [mW]	θ_{start} [°C]	θ_{high} [°C]	$\Delta\theta$ [°C]
Vacuum	155 ± 3	23.431 ± 0.045	26.92 ± 0.11	3.49 ± 0.25
	533 ± 3	23.76 ± 0.05	34.599 ± 0.013	10.84 ± 0.21
	794 ± 5	24.06 ± 0.03	40.41 ± 0.05	16.36 ± 0.28
Ambient pressure	154 ± 5	20.916 ± 0.024	22.267 ± 0.012	1.35 ± 0.12
	541 ± 5	20.832 ± 0.035	25.426 ± 0.011	4.59 ± 0.15
	810 ± 7	20.634 ± 0.035	27.555 ± 0.036	6.92 ± 0.19

The uncertainties shown for θ_{start} and θ_{high} are taken from the covariance matrix of the fit parameters. These are added to the errors determined in the previous section to get the uncertainties of the temperature differences shown in Table 6.2. The temperature differences are higher for vacuum conditions, as expected. At the maximum tested power, the difference of differences between vacuum and ambient pressure is (9.44 ± 0.47) °C.

6.4.3 Thermal pictures

Complementary to the temperature measurement, thermographic images (hereafter also referred to as infrared images) were taken from the laser mirror at different stages of the experiment. To comprehend these pictures, Fig. 6.8 shows the view through the ZnSe window. Angle and tilt were chosen to match the infrared images. In the upper right corner the port of the turbopump is visible.

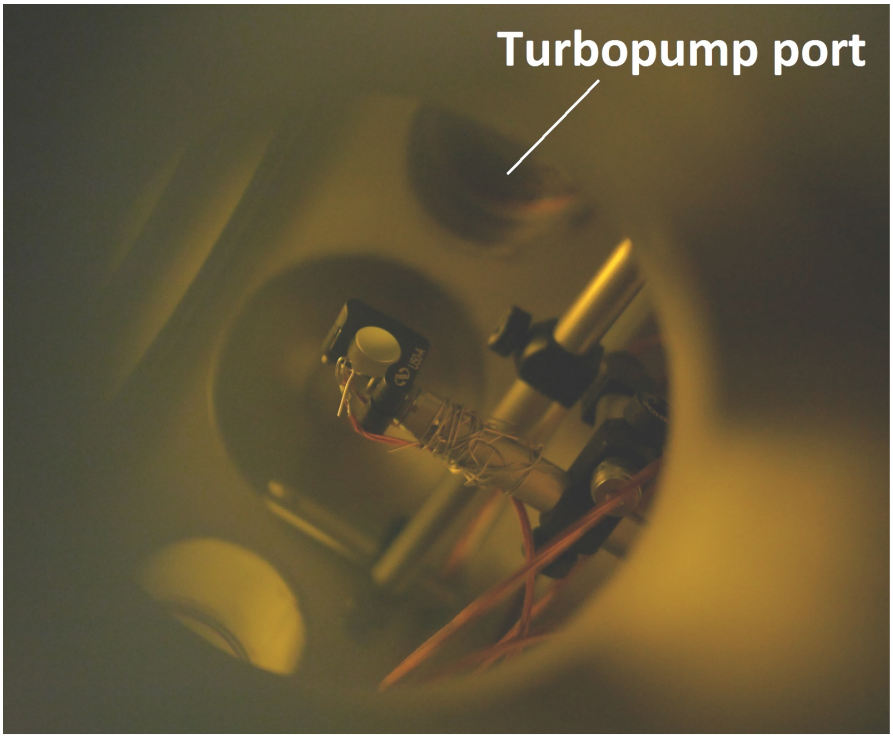

Figure 6.8: Tilted view through the ZnSe window. The turbopump port is visible at the upper right corner. The angle and tilt of this image was chosen to match the infrared-camera pictures.

Fig. 6.9 and 6.10 show pictures taken with the infrared-camera during the vacuum measurement series. Fig. 6.9 was taken right before the laser beam was unblocked to record the highest-laser power data. The mirror thus reached a steady temperature. Mirror and its mount are barely recognizable in Fig. 6.9. Instead, it is noticeable that there is significant radiation from the turbopump which heats up due to friction. In comparison, Fig. 6.10 shows a picture of the hottest state during

the experiment. Notice that the color scaling is different for both pictures. Fig. 6.10 was taken during the vacuum measurement series and the highest incident laser power. The components reached a steady-state temperature when the picture was recorded. In contrast to the low temperature steady-state, the mirror and its mount are clearly visible in the hot state. Remarkably, the reflective aluminum surface emits a lot less thermal radiation than the side surface. The mirror mount radiates less than the mirror side but more than the aluminum surface. The emissivities in the camera were set to $\varepsilon = 0.85$ (cf. Sec. 6.4.4).
In Fig. 6.11 a picture of the hottest measured temperature during the ambient pressure series is depicted. Generally, less radiation from the components is visible due to the lower temperature. Additionally, the radiation from the turbopump is not visible anymore.

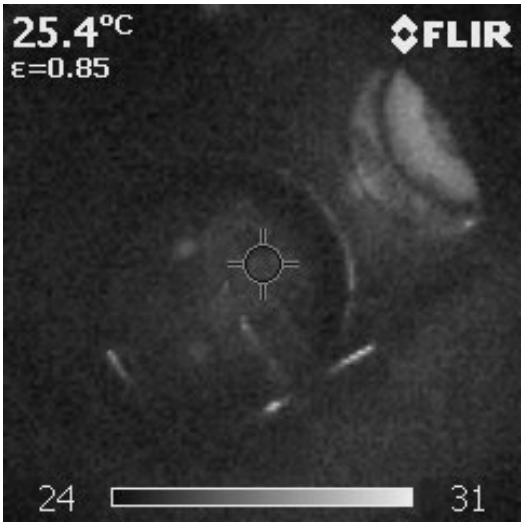

Figure 6.9: Thermographic picture with turbopump turned on and laser blocked. The steady-state temperature of the mirror has been reached.

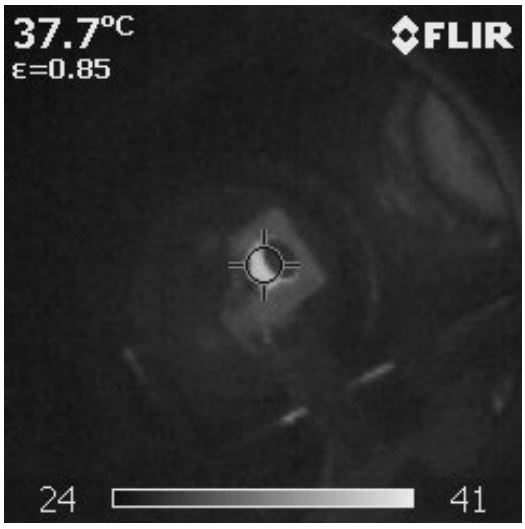

Figure 6.10: Thermographic picture with turbopump turned on and laser unblocked. The laser power was (794 ± 5) mW. The steady-state temperature of the mirror has been reached.

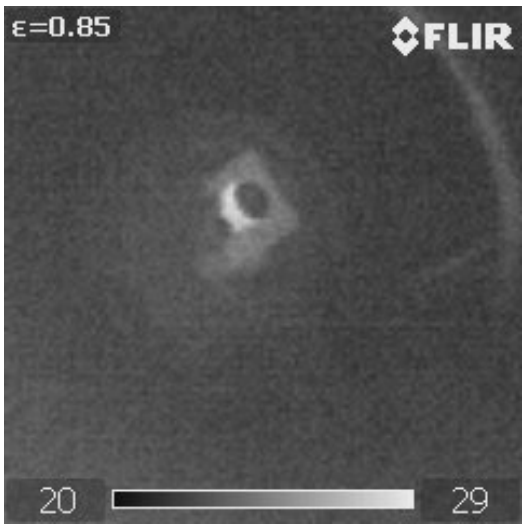

Figure 6.11: Thermographic picture with turbopump turned off and laser unblocked. The laser power was (810 ± 7) mW. The steady-state temperature of the mirror has been reached.

6.4.4 Determining emissivity of mirror surfaces and estimating radiative heat transfer

Since the temperature of the emitting body was known, the emissivity ε of the surfaces could be estimated by changing ε in the IR-camera settings until the display showed the same temperature as the contact measurement. This is of course a coarse determination due to the small area of the emitting surfaces. For the strongly emitting side of the mirror $\varepsilon_{\text{side}} = 0.85 \pm 0.08$ was found. The value for the weakly thermally radiating aluminum surface was estimated to be $\varepsilon_{\text{aluminum}} = 0.41 \pm 0.10$. Using Eq. 2.6 one can now calculate the net heat transfer by radiation in vacuum. This yields, for the highest measured temperature,

$$\begin{aligned} P_{\text{net,side and back surface}} &= (54 \pm 14)\,\text{mW} \\ P_{\text{net,front surface}} &= (5.5 \pm 2.4)\,\text{mW}, \end{aligned} \tag{6.9}$$

where it was assumed that the back of the mirror shows the same emissivity than the side. The enlarged surface due to the sensor glued to the back side was neglected. The absorbed heat rate at this condition is $(88 \pm 30)\,\text{mW}$. Therefore, between 36 % and 100 % of the absorbed laser power is emitted by radiation of the mirror alone. Since we clearly see that the mount also thermally radiates we can conclude that the amount of heat removed by conduction through the post is negligible. This also explains that the posts show no thermal radiation on the pictures above.

Estimation of temperatures of cavity mirrors

Except for the In-coupling mirror, the cavity mirrors are coated with a high-reflectivity coating. The manufacturer claims a reflectivity of 99.996% and a transmissivity of 0.004% indicating no absorption at all. On the other hand, the laser powers in the cavity are much higher than the powers used in the test measurements, so that even a very small fraction of absorption can lead to significant heating rates. If we assume an absorption of 0.0001% and an intra-cavity power of 6 kW, corresponding to a typical value, the absorbed energy rates at the high-reflectivity mirrors are 6 mW which is lower than the lowest rate we tested with ($\approx 17\,\text{mW}$). In this case, the temperature increase is smaller than 4 °C and tolerable for the experiment.

7 Discussion

The assembly of temperature detector, wires and mirror was flawed. Especially the Kapton wires for use in vacuum proved to be challenging since they had a large cross-section and were accordingly stiff. When attaching these to the small connecting wires of the sensor, the latter were bended and mechanical stress exerted at the point where the connecting wire enter the component sealing of the sensor. The manufacturer advises to avoid this since the sensor might break and there can be systematic shifts of the resistance, distorting the measurement [20]. To apply the temperature measurement employed in this work, it is necessary to improve the manufacturing technique. One possibility might be to use detachable connections such as plugs and using more flexible wires to keep the sensor wires stress-free. On the other hand, one could devise supporting structures for the stiff Kapton wires. Additionally, the soldering itself was difficult due to the fact that 3 wires needed to be connected at a single point for the 4-wire circuit and the small size of the sensor. A solution could be to crimp or even weld these connections.
The accuracy of the temperature measurement can be further increased by calibrating the sensors. This would restrict the total absolute error as well as the error differences since the deviations as a function of temperature could be determined. However, this requires to have an accurate reference measurement and the effort is probably larger than the benefit. Alternatively, one could also measure the resistance of the reference resistor with greater precision. A measurement with an uncertainty of less than 0.05% should be possible. Further possibilities to enhance the performance of the temperature measurement are given by using sensors with tightened tolerances or to use an ADC with improved resolution. It is even possible to calibrate the ADC to eliminate gain- and offset errors. Ultimately however, the performance of a RTD measurement is limited by the detector.
Regarding the actual cooling system, there is room for improvement especially at the thermal connection between mirrors and large copper braids. The design presented in this work plans to glue thin foil directly at the mirror's side surface or to a component close to the mirror and guide the heat through this foil to the large copper braid (apart from the grating-mirror). As elucidated in Sec. 5.3 this requires the distance between husk of large braid and mirror to be small in order to keep the temperature of the mirrors low. In turn, this restricts the position of the steel tables to stand close to the mirror mounts, making the whole arrangement rather inflexible. Additionally, the foil is glued to the mirrors so that it is tedious to remove single mirrors. This might be improved if the foil is clamped to the mirror

side. Unfortunately, the temperature drop at the interface due to thermal contact conductance is expected to increase in this case (cf. Sec. 2.4). If the actual heat loads turn out to be much lower than the values used here, clamping the foil to the mirrors instead of gluing might still provide enough cooling. Additionally, the cross-section of the copper between mirror and large braid could also be increased by using more massive material and an improved geometry. In this case, the length-restriction is less critical and more flexibility is preserved in positioning the steel tables.
On the other hand, if the heat loads are even larger than estimated or thermal contact resistance causes the temperature differences to be too great, despite large cross-sections, it can also be thought about designing special mirror mounts. These could be manufactured in such a way that a heat conducting material can be clamped more firmly to the side face of the mirrors. An even more elaborate cooling technique could consist of individual peltier elements positioned close to the mirrors and regulating each mirror's temperature. Most probably however, this is not practical.
Lastly, regarding the calculation formula (Eq. 2.62), which was used to compute the necessary cross-sections, it is unclear whether the solution to the steady-state of the heat equation, given by Eq. 2.62, holds for arbitrary 3-dimensional geometries with constant cross-section. Therefore, it is doubtful whether Eq. 2.62 gives the correct relation between cross-section, length, power, temperature difference and heat conductivity. This might need further investigation. Intuitively however, the difference for curved geometries compared to flat geometries stems from the fact that the temperature distribution across the cross-section is not uniform anymore. Especially for small radii Eq. 2.62 should be a good description.

8 Conclusion and Outlook

This work was intended to design a cooling system for mirrors of an enhancement cavity in a vacuum chamber. To realize this, individual components as well as assemblies were designed using the software 'Solidworks' [41]. The system transports heat from devices in the vacuum chamber by conduction through various copper bodies to stainless steel tubes. Cooling water flows through the tubes, thereby removing the heat. The tubes are situated in the vacuum chamber. Additionally to the cooling system itself, several peripheral components were designed. After development, the system and additional components were commissioned at the on-site workshop of the Max Planck Institute for Nuclear Physics in Heidelberg, where they are currently under construction. The system is expected to remove a heat load of 0.2 mW from each mirror while limiting the temperature increase to less than 10 K. Since the mirrors are manufactured from low expansion material, this increase is tolerable.

Complementarily to the cooling system, a special framework for temperature measurement of small components in ultra-high vacuum conditions was composed. A Pt1000 chip-sensor is used as detector. It is read out by a microcontroller, using a 4-wire circuit and a reference resistor. The sensor is glued to the device, whose temperature should be measured. Error analysis of the temperature measurement was carried out.

To test the temperature measurement and measure the heating of mirrors due to absorption of laser light, a preliminary measurement was conducted. In a test vacuum chamber, a metallic mirror was irradiated by laser light. The temperature increase due to the absorption was measured for different laser powers. For comparison, the measurements were carried out consecutively in high vacuum and at ambient pressure. The temperature increase in vacuum conditions was significantly higher than at ambient pressure, showing the influence of convection. Additionally, thermal radiation of the components was examined by employing an infrared camera. The side surface of the mirror radiated most intensively. The net transferred heat by radiation in vacuum was estimated to be (59.5 ± 16.4) mW for the highest temperature measured, indicating that the heat transfer is dominated by radiation. Since no radiation of the posts was detectable, the heat is emitted mostly by mirror and mount. Therefore, heat conduction for this configuration is negligible.

The cooling system is currently under construction in the on-site workshop. Once

it has been implemented, test measurements using the developed temperature acquisition system can be conducted. This allows for example to determine the heat load of the mirrors by measuring the temperature difference for a fixed length of one of the large braids, since cross-sections of these are known. Alternatively, the temperature measurement system can be used to measure arbitrary temperatures inside and outside the vacuum chamber. The connections of the cavity mirrors to the large copper braids might be improved in the future. After this has been done, the cooling system hopefully enables long-term stable operation of the enhancement cavity, thereby realizing a frequency comb in the XUV and enabling high precision spectroscopy of highly-charged ions.

Sources and References

[1] M. S. Safronova et al. “Search for new physics with atoms and molecules”. In: *Rev. Mod. Phys.* 90 (2 June 2018), p. 025008. DOI: 10.1103/RevModPhys.90.025008. URL: https://link.aps.org/doi/10.1103/RevModPhys.90.025008.

[2] M. G. Kozlov et al. “Highly charged ions: Optical clocks and applications in fundamental physics”. In: *Rev. Mod. Phys.* 90 (4 December 2018), p. 045005. DOI: 10.1103/RevModPhys.90.045005. URL: https://link.aps.org/doi/10.1103/RevModPhys.90.045005.

[3] J. Michael Shull, Britton D. Smith and Charles W. Danforth. “THE BARYON CENSUS IN A MULTIPHASE INTERGALACTIC MEDIUM: 30% OF THE BARYONS MAY STILL BE MISSING”. In: *The Astrophysical Journal* 759.1 (October 2012), p. 23. DOI: 10.1088/0004-637x/759/1/23. URL: https://doi.org/10.1088%2F0004-637x%2F759%2F1%2F23.

[4] Jun Ye et al. *Femtosecond Optical Frequency Comb: Principle, Operation, and Applications*. Ed. by Jun Ye and Steven T. Cundiff. Norwell, MA: Kluwer Academic Publishers / Springer, 2005.

[5] Theodor W. Hänsch. “Nobel Lecture: Passion for precision”. In: *Rev. Mod. Phys.* 78 (4 November 2006), pp. 1297–1309. DOI: 10.1103/RevModPhys.78.1297. URL: https://link.aps.org/doi/10.1103/RevModPhys.78.1297.

[6] Carsten Winterfeldt, Christian Spielmann and Gustav Gerber. “Colloquium: Optimal control of high-harmonic generation”. In: *Rev. Mod. Phys.* 80 (1 January 2008), pp. 117–140. DOI: 10.1103/RevModPhys.80.117. URL: https://link.aps.org/doi/10.1103/RevModPhys.80.117.

[7] Christoph Gohle et al. “A frequency comb in the extreme ultraviolet”. In: *Nature* 436 (7048 July 2005), pp. 234–237. DOI: doi:10.1038/nature03851. URL: https://www.nature.com/articles/nature03851.

[8] Max Planck. “Zur Theorie des Gesetzes der Energieverteilung im Normalspectrum”. In: *Verhandlungen der deutschen physikalischen Gesellschaft* (2 14th December 1900), pp. 237–245.

[9] Max Planck. “Ueber das Gesetz der Energieverteilung im Normalspectrum”. In: *Annalen der Physik* 309 (3 1901), pp. 553–563.

[10] Hans Dieter Baehr and Karl Stephan. *Wärme- und Stoffübertragung*. 9th ed. Berlin, Heidelberg: Springer Vieweg, 2016.

[11] Peter von Böckh and Thomas Wetzel. *Wärmeübertragung. Grundlagen und Praxis*. 7th ed. Berlin, Heidelberg: Springer Vieweg, 2017.

[12] Klaus Stierstadt. *Thermodynamik für das Bachelorstudium*. 2nd ed. Berlin: Springer Spektrum, 2018.

[13] Werner Stadlmayr. *Thermodynamik-nicht nur für Nerds. Grundlagen der Thermodynamik mit Übungen und Beispielen*. 1st ed. Wiesbaden: Springer Vieweg, 2018.

[14] Matthew J. Hancock. *The 1-D Heat equation*. 2006. URL: https://pdfs.semanticscholar.org/0e31/9ff7d1f0833e6f084255fcd89f06167f00c4.pdf (visited on 13th August 2019).

[15] Deutsches Kupferinstitut. *Cu-ETP Datenblatt*. 2005. URL: https://www.kupferinstitut.de/fileadmin/user_upload/kupferinstitut.de/de/Documents/Shop/Verlag/Downloads/Werkstoffe/Datenblaetter/Kupfer/Cu-ETP.pdf (visited on 16th August 2019).

[16] Chakravarti V. Madhusudana. *Thermal Contact Conductance*. 2nd ed. Heidelberg, New York: Springer International Publishing, 2014.

[17] Rainer Parthier. *Messtechnik. Grundlagen und Anwendungen der elektrischen Messtechnik*. 8th ed. Wiesbaden: Springer Vieweg, 2016.

[18] Jerry Janesch. *Two-wire vs. four-wire resistance measurements*. URL: https://www.edn.com/design/test-and-measurement/4411117/Two-wire-vs--four-wire-resistance-measurements (visited on 12th September 2019).

[19] Jerry Janesch. *Two-wire vs. four-wire resistance measurements*. URL: https://www.edn.com/design/test-and-measurement/4411117/2/Two-wire-vs--four-wire-resistance-measurements (visited on 12th September 2019).

[20] JUMO GmbH & Co. KG. *Application Notes for Platinum-Chip Temperature Sensors*. URL: https://www.jumo.de/attachments/JUMO/attachmentdownload?id=3386&filename=b90.6121.4en.pdf (visited on 23rd August 2019).

[21] JUMO GmbH & Co. KG. *Construction and application of platinum temperature sensors*. URL: https://www.jumo.de/attachments/JUMO/attachmentdownload?id=3008&filename=t90.6000gb.pdf (visited on 23rd August 2019).

[22] MenloSystems. *FC1000*. URL: https://www.menlosystems.com/assets/datasheets/MENLO_FC1000-250-_D-EN-2017-09_3w.pdf (visited on 29th August 2019).

[23] Jan-Hendrik Oelmann. "Schematic overview of the laser system". 2019.

[24] Janko Nauta et al. “Towards precision measurements on highly charged ions using a high harmonic generation frequency comb”. In: *Nuclear Instruments and Methods in Physics Research Section B: Beam Interactions with Materials and Atoms* 408 (2017). Proceedings of the 18th International Conference on the Physics of Highly Charged Ions (HCI-2016), Kielce, Poland, 11-16 September 2016, pp. 285–288. ISSN: 0168-583X. DOI: https://doi.org/10.1016/j.nimb.2017.04.077. URL: http://www.sciencedirect.com/science/article/pii/S0168583X17305281.

[25] Jan-Hendrik Oelmann, Janko Nauta and Jose Crespo. *HGSFP Poster Presentation*. Poster. 2019.

[26] Eric D. Black. “An introduction to Pound–Drever–Hall laser frequency stabilization”. In: *American Journal of Physics* 69.1 (2001), pp. 79–87. DOI: 10.1119/1.1286663. URL: https://doi.org/10.1119/1.1286663.

[27] JULABO USA Inc. *Operating manual. Refrigerated and Heating Circulators*. F12-MC F25-MC F26-MC F32-MC F33-MC F34-MC FS18-MC FP40-MC FP50-MC FPW50-MC. 2nd February 2005.

[28] Druseidt Elektrotechnische Spezialfabrik GmbH & Co KG. *Earthing tapes-and connectors*. 2019. URL: https://www1.druseidt.de/englisch/produkte/flexible_verbindungen/untermenue/c.html (visited on 16th August 2019).

[29] Kurt J. Lesker Company. *Torr Seal Specifications*. URL: https://www.lesker.com/newweb/fluids/pdf/torrsealspecifications.pdf (visited on 16th August 2019).

[30] M&I Materials Ltd. *Apiezon L,M & N greases. Ultra High and High Vacuum Greases*. URL: https://static.mimaterials.com//apiezon/DocumentLibrary/TechnicalDatasheets/Apiezon_L_M_and_N_Ultra_High_and_High_Vacuum_Greases_Datasheet.pdf (visited on 16th August 2019).

[31] Thorlabs. *UV-Enhanced Aluminum Mirrors*. URL: https://www.thorlabs.com/newgrouppage9.cfm?objectgroup_id=12393&pn=PF05-03-F01 (visited on 10th September 2019).

[32] JUMO GmbH & Co. KG. *Platinum-chip temperature sensors with connecting wires to EN 60 751*. URL: https://www.distrelec.de/Web/Downloads/en/_e/qcJUMO-Platin-Chip-tempsensoren_e.pdf (visited on 22nd August 2019).

[33] Maxim Integrated. *MAX31865. RTD-to-Digital Converter*. URL: https://datasheets.maximintegrated.com/en/ds/MAX31865.pdf (visited on 23rd August 2019).

[34] CJMCU. *CJMCU 31865*. URL: https://www.aliexpress.com/item/32816733537.html?spm=a2g0s.9042311.0.0.66d84c4dLZZMf4 (visited on 9th September 2019).

[35] Arduino. *Arduino MKR ZERO*. URL: https://store.arduino.cc/arduino-mkrzero (visited on 26th August 2019).

[36] Panasonic. *Metal Film (Thin Film) Chip Resistors, High Reliability Type 0201, 0402, 0603, 0805, 1206*. URL: https://docs-emea.rs-online.com/webdocs/0d01/0900766b80d019df.pdf (visited on 26th August 2019).

[37] Allectra GmbH. *220 CM Feedthroughs*. URL: https://shop.allectra.com/documents/peMAKjSESYt86aTdJdCfFN2KNpt3FrBg8ZbWELrY.pdf/download?force=1 (visited on 26th August 2019).

[38] Allectra GmbH. *Kapton insulated wires for UHV use*. URL: https://shop.allectra.com/documents/9c5d682363a7dc8a6e63499c12eaa71e.pdf/download?force=1 (visited on 26th August 2019).

[39] D. Boguhn and M. Koepke. "Typical R(T90) Characteristics of Platinum Thin-Film Resistance Thermometers in the Temperature Range from -50 °C to +660 °C". In: *International Journal of Thermophysics* 32.11 (December 2011), pp. 2379–2387. DOI: 10.1007/s10765-011-1088-6. URL: https://doi.org/10.1007/s10765-011-1088-6.

[40] Maxim Integrated. *The ABCs of ADCs. Understanding How ADC Errors Affect System Performance*. URL: https://www.maximintegrated.com/en/app-notes/index.mvp/id/748 (visited on 9th September 2019).

[41] Dassault Systems. *Solidworks*. URL: https://www.solidworks.com/de (visited on 12th September 2019).

[42] Reinhard Lerch. *Elektrische Messtechnik. Analoge, digitale und computergestützte Verfahren*. 7th ed. Berlin, Heidelberg: Springer Vieweg, 2016.

[43] Ekbert Hering and Gert Schönfelder. *Sensoren in Wissenschaft und Technik. Funktionsweise und Einsatzgebiete*. 2nd ed. Wiesbaden: Springer Vieweg, 2018.

[44] *Copper*. 2019. URL: https://en.wikipedia.org/wiki/Copper (visited on 16th August 2019).

[45] Andrei Derevianko, V. A. Dzuba and V. V. Flambaum. "Highly Charged Ions as a Basis of Optical Atomic Clockwork of Exceptional Accuracy". In: *Phys. Rev. Lett.* 109 (18 October 2012), p. 180801. DOI: 10.1103/PhysRevLett.109.180801. URL: https://link.aps.org/doi/10.1103/PhysRevLett.109.180801.

[46] J. C. Berengut, V. A. Dzuba and V. V. Flambaum. “Enhanced Laboratory Sensitivity to Variation of the Fine-Structure Constant using Highly Charged Ions”. In: *Phys. Rev. Lett.* 105 (12 September 2010), p. 120801. DOI: 10.1103/PhysRevLett.105.120801. URL: https://link.aps.org/doi/10.1103/PhysRevLett.105.120801.

Attachments

- Solidworks-Drawing: Weld subassembly
- Solidworks-Drawing: 180° bended tube
- Solidworks-Drawing: Special CF50 flange
- Solidworks-Drawing: CF63 and CF50 assembly
- Solidworks-Drawing: Entry tube with dual bends
- Solidworks-Drawing: Small foot
- Solidworks-Drawing: Long foot
- Solidworks-Drawing: Modified CF 63 blind flange
- Solidworks-Drawing: Weld subassembly
- Solidworks-Drawing: New lid for chamber with weld-on flanges
- Solidworks-Drawing: New lid
- Solidworks-Drawing: CF100-40 reducer flange with threaded holes
- Solidworks-Drawing: Steel table short
- Solidworks-Drawing: Steel table long
- Solidworks-Drawing: Strut rear
- Solidworks-Drawing: Strut front
- Solidworks-Drawing: Strut front foot
- Solidworks-Drawing: Copper block 1
- Solidworks-Drawing: Copper block 2
- Solidworks-Drawing: Copper block 3

Erklärung

Ich versichere, dass ich diese Arbeit selbstständig verfasst und keine anderen als die angegebenen Quellen und Hilfsmittel benutzt habe.

Heidelberg, den 12.09.2019

Jakob Krummeich